




## Article

# Redox-Switchable Behavior of Transition-Metal Complexes Supported by Amino-Decorated N-Heterocyclic Carbenes

Mirko Ruamps <sup>1</sup>, Stéphanie Bastin <sup>1</sup> , Lionel Rechinat <sup>1</sup>, Alix Sournia-Saquet <sup>1</sup> , Laure Vendier <sup>1</sup>, Noël Lugan <sup>1</sup>, Jean-Marie Mouesca <sup>2</sup>, Dmitry A. Valyaev <sup>1,\*</sup>, Vincent Maurel <sup>2,\*</sup> and Vincent César <sup>1,\*</sup> 

<sup>1</sup> LCC-CNRS, Université de Toulouse, CNRS, 31077 Toulouse, France; mirko.ruamps@gmail.com (M.R.); stephanie.bastin@lcc-toulouse.fr (S.B.); lionel.rechinat@lcc-toulouse.fr (L.R.); alix.saquet@lcc-toulouse.fr (A.S.-S.); laure.vendier@lcc-toulouse.fr (L.V.); noel.lugan@laposte.net (N.L.)

<sup>2</sup> Université Grenoble Alpes, CEA, CNRS, IRIG, SyMMES, 38000 Grenoble, France; jean-marie.mouesca@cea.fr

\* Correspondence: dmitry.valyaev@lcc-toulouse.fr (D.A.V.); vincent.maurel@cea.fr (V.M.); vincent.cesar@lcc-toulouse.fr (V.C.)

**Abstract:** The coordination chemistry of the N-heterocyclic carbene ligand  $\text{IMes}^{(\text{NMe}_2)_2}$ , derived from the well-known IMes ligand by substitution of the carbenic heterocycle with two dimethylamino groups, was investigated with  $d^6$  [Mn(I), Fe(II)],  $d^8$  [Rh(I)], and  $d^{10}$  [Cu(I)] transition-metal centers. The redox behavior of the resulting organometallic complexes was studied through a combined experimental/theoretical study, involving electrochemistry, EPR spectroscopy, and DFT calculations. While the complexes  $[\text{CuCl}(\text{IMes}^{(\text{NMe}_2)_2})]$ ,  $[\text{RhCl}(\text{COD})(\text{IMes}^{(\text{NMe}_2)_2})]$ , and  $[\text{FeCp}(\text{CO})_2(\text{IMes}^{(\text{NMe}_2)_2})](\text{BF}_4)$  exhibit two oxidation waves, the first oxidation wave is fully reversible but only for the first complex the second oxidation wave is reversible. The mono-oxidation event for these complexes occurs on the NHC ligand, with a spin density mainly located on the diaminoethylene NHC-backbone, and has a dramatic effect on the donating properties of the NHC ligand. Conversely, as the Mn(I) center in the complex  $[\text{MnCp}(\text{CO})_2(\text{IMes}^{(\text{NMe}_2)_2})]$  is easily oxidizable, the latter complex is first oxidized on the metal center to form the corresponding cationic Mn(II) complex, and the NHC ligand is oxidized in a second reversible oxidation wave.

**Keywords:** redox-active ligands; N-heterocyclic carbene; organometallic complexes; EPR spectroscopy; DFT calculations



**Citation:** Ruamps, M.; Bastin, S.; Rechinat, L.; Sournia-Saquet, A.; Vendier, L.; Lugan, N.; Mouesca, J.-M.; Valyaev, D.A.; Maurel, V.; César, V. Redox-Switchable Behavior of Transition-Metal Complexes Supported by Amino-Decorated N-Heterocyclic Carbenes. *Molecules* **2022**, *27*, 3776. <https://doi.org/10.3390/molecules27123776>

Academic Editor: Artem L. Gushchin

Received: 25 May 2022

Accepted: 8 June 2022

Published: 11 June 2022

**Publisher's Note:** MDPI stays neutral with regard to jurisdictional claims in published maps and institutional affiliations.



**Copyright:** © 2022 by the authors. Licensee MDPI, Basel, Switzerland. This article is an open access article distributed under the terms and conditions of the Creative Commons Attribution (CC BY) license (<https://creativecommons.org/licenses/by/4.0/>).

## 1. Introduction

Since the isolation of the first free N-heterocyclic carbene (NHC) by Arduengo in 1991 [1], and the pioneering work of Herrmann in homogeneous catalysis as early as 1995 [2], NHCs were established as privileged ligands in organometallic chemistry and catalysis [3–7], and NHC-complexes found various promising applications as photoluminescent species [8] and metallodrugs [9], or in material chemistry [10]. This remarkable development was mainly driven by the aptitude of NHC ligands to stabilize transition metals in a wide range of oxidation states, due to their strong electronic donation properties, and to the good steric protection they offer [11,12]. Interestingly, while NHCs were first considered as fully innocent, pure-spectator ligands, the seminal report by Tumanskii and Apeloig in 2007 shows that imidazole-derived NHC ligands are also able to accept and delocalize radicals, or some spin density, within their heterocyclic scaffold [13], and, hence, that they could also be considered as redox-active ligands [14–18]. In parallel, redox-active NHC ligands were designed on purpose, by combining the carbenic heterocycle with some known redox-active moieties, such as ferrocene [19–22], cobaltocenium [23], quinone [24–26], *o*-aminophenols [27–31], or more recently, a naphthalene diimide backbone [32,33]. The redox-active NHC ligands allowed the design of redox-switchable catalysts by a strong modification of the electronic properties through a redox stimulus [7,34], or permitted the access to multiple oxidation states of the complexes.

We entered this area of chemistry in 2018, by reporting preliminary studies on the redox behavior of the thiourea  $A^{NMe_2}$  and  $A^{(NMe_2)_2}$ , derived from the mono-substituted 4-(dimethylamino)imidazol-2-ylidene  $IMes^{NMe_2}$  and the di-substituted 4,5-bis(dimethylamino)imidazol-2-ylidene  $IMes^{(NMe_2)_2}$ , respectively (Figure 1) [35]. While we studied the latter amino-derived NHCs mainly in the direction of organometallic catalysis with remarkable results [36–40], we actually initiated this program by considering the analogy between the NHC backbones and the electron-rich tri- and tetra-aminoethylene moieties, which are well-known electron-rich reducing agents [41,42]. We indeed show that both thioureas are redox-active, due to the presence of the dimethylamino groups onto their backbone. While  $A^{NMe_2}$  can be oxidized mono-electronically to the corresponding persistent radical-cation  $[A^{NMe_2}]^{\bullet+}$ ,  $A^{(NMe_2)_2}$  exhibits two oxidized forms, namely, the radical cation  $[A^{(NMe_2)_2}]^{\bullet+}$  and the diamagnetic dication  $[A^{(NMe_2)_2}]^{2+}$  and both are remarkably stable. Thus, we decided to extend this study to the case of the transition-metal complexes of the diamino-substituted  $IMes^{(NMe_2)_2}$  ligand (**1**), and we report herein that this NHC ligand exhibits redox-active behavior with a variety of metal centers.

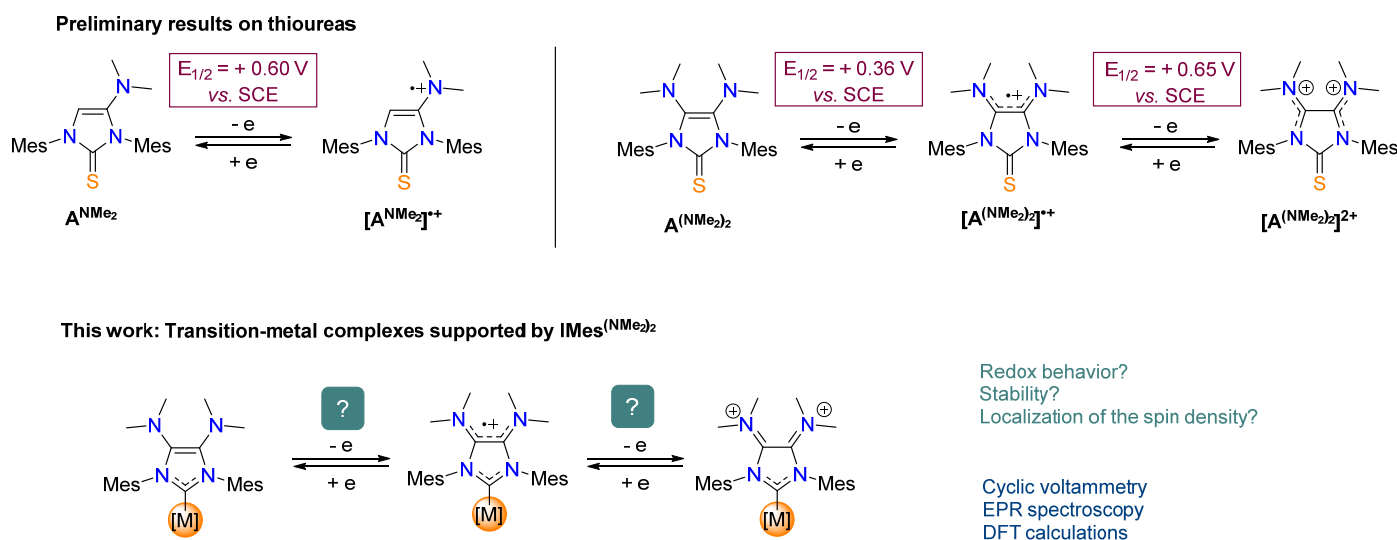


**Figure 1.** Redox behaviors of the thiourea  $A^{NMe_2}$  and  $A^{(NMe_2)_2}$  derived from the amino-decorated  $IMes^{NMe_2}$  and  $IMes^{(NMe_2)_2}$ , respectively, and of the transition-metal complexes of  $IMes^{(NMe_2)_2}$ , subject of the present study.

## 2. Results and Discussion

### 2.1. Redox Properties of $IMes^{(NMe_2)_2}$ Copper(I) Complex **2**

We started our investigation by studying the behavior of the copper(I) complex  $[CuCl(\mathbf{1})]$  (**2**), which is synthesized by reacting the free stable NHC **1**, generated from  $\mathbf{1} \cdot HOTf$  by deprotonation with one equivalent of potassium bis(trimethylsilyl)amide (KHMDs), with an excess of  $CuCl$  and  $NaCl$  at room temperature (Figure 2a). These unusual conditions are necessary to avoid the competitive formation of the cationic homoleptic complex  $[Cu(\mathbf{1})_2]^+$  under standard conditions (1 equivalent of  $CuCl$ ) [43]. The  $^1H$  NMR spectrum of **2** is particularly simple, as only four singlets are observed, due to the  $C_{2v}$  symmetry of the molecule, and to the equivalence of the twelve protons of the  $NMe_2$  substituents, as already observed in the previous complexes of ligand **1** [36,39,40]. The redox behavior of complex **2** was first examined by cyclic voltammetry (CV) measurements (Figure 2b), and compared to the parent unsubstituted complex  $[CuCl(IMes)]$  (Figure S1). While complex  $[CuCl(IMes)]$  displays no clear oxidation wave, the bis-amino-substituted complex **2** features two fully reversible one-electron transfer processes at  $E_{1/2} = +0.71$  V, and +1.11 V vs. SCE. This CV pattern is highly similar to that observed for the corresponding thiourea  $A^{(NMe_2)_2}$  [35], with the exception that both oxidation processes in **2** occur at higher potentials. This suggests that the redox events in complex **2**

might also be located on the NHC ligand, and prompted us to explore in more detail the mono- and di-oxidized complexes  $[2]^+$  and  $[2]^{2+}$ .

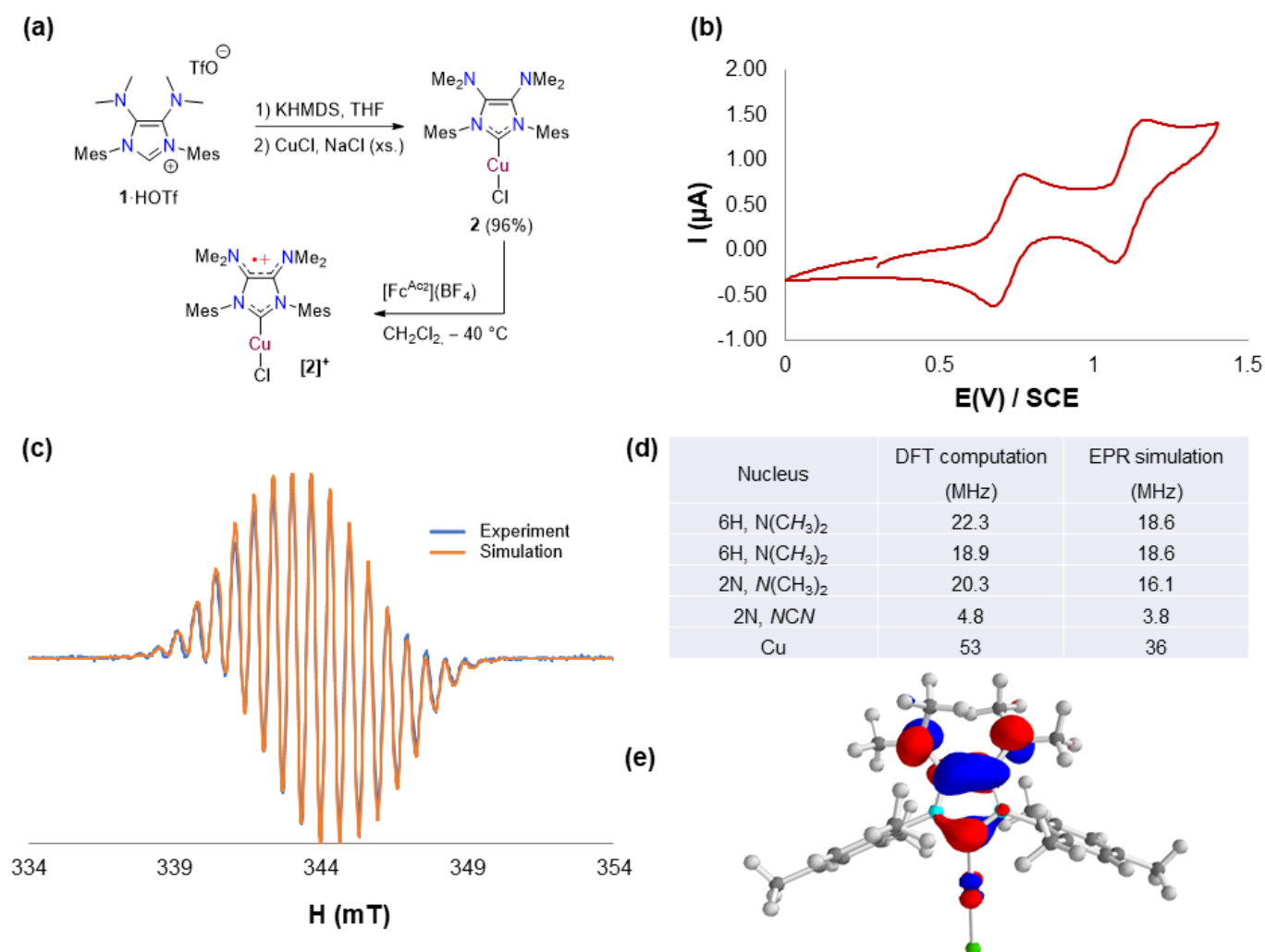


**Figure 2.** (a) Synthesis of complex **2** and subsequent chemical oxidation reaction to form  $[2]^+$ . (b) Cyclic voltammogram of complex **2** (Pt working electrode, 1 mM in  $\text{CH}_2\text{Cl}_2$  with 0.1 M  $\text{Bu}_4\text{NPF}_6$  as the supporting electrolyte,  $200 \text{ mV} \cdot \text{s}^{-1}$  scan rate; potentials are calibrated against  $\text{Fc}/\text{Fc}^+$  as internal standard with  $E_{1/2}(\text{Fc}/\text{Fc}^+) = +0.46 \text{ V vs. SCE}$ ). (c) X-band EPR spectrum of  $[2]^+$  in  $\text{CH}_2\text{Cl}_2$ /toluene solution (1:1) at room temperature: microwave frequency = 9.6508 GHz, mod. ampl. = 0.1 mT, power = 2 mW. Simulation parameters:  $g_{\text{iso}} = 2.00338$ ,  $lw = 0.05 + 0.1 \text{ mT}$  (Gaussian + Lorentzian) (d) Isotropic hyperfine coupling constants obtained by DFT computation and by simulation. (e) DFT-optimized structure of  $[2]^+$ , and representation of the SOMO (isodensity value of 0.05 a.u.).

Complex **2** was chemically oxidized using an equimolar amount of 1,1'-diacetylferrocenium tetrafluoroborate ( $[\text{Fc}^{\text{Ac}2}](\text{BF}_4)$ ,  $E_{1/2} = +0.95 \text{ V}$  [44]) in  $\text{CH}_2\text{Cl}_2$  at  $-40 \text{ }^\circ\text{C}$ , to give a deep blue solution of the one-electron oxidized species  $[2]^+$ , which was characterized immediately by EPR spectroscopy at room temperature in  $\text{CH}_2\text{Cl}_2$ /toluene (1:1) solution (Figure 2c). The X-band EPR spectrum of  $[2]^+$  is consistent with a delocalized organic radical (Landé factor of  $g_{\text{iso}} = 2.00338$ ), and displays a symmetrical, hyperfine splitting pattern. The simulated spectrum fits perfectly with the experimental spectrum, and is composed mainly of hyperfine interactions between the radical and twelve equivalent protons ( $a_{\text{H}} = 18.6 \text{ MHz}$ ), with the two exocyclic nitrogen atoms ( $a_{\text{N}} = 16.1 \text{ MHz}$ ) and with the copper center ( $a_{\text{Cu}} = 36 \text{ MHz}$ ), and, to a lower extent, by a hyperfine coupling constant with the two nitrogen atoms of the diaminocarbene unit ( $a_{\text{N}} = 3.8 \text{ MHz}$ ) (Figure 2d). The optimized geometry computed by DFT

for  $[2]^{•+}$  confirms that the copper center remains linear and dicoordinate, which is in agreement with a Cu(I) center, and shows, in particular, a planarization of the two exocyclic nitrogen atoms ( $\Sigma_N = 359.5^\circ$  and  $359.6^\circ$ ), with a twist of the NMe<sub>2</sub> plane relative to the carbenic heterocycle of ca.  $34^\circ$ , most probably due to steric congestion, as already encountered in the related thiourea derivative  $[A^{(NMe_2)_2}]^{•+}$ . Similarly, the SOMO orbital of  $[2]^+$  is mainly localized on the bis(dimethylamino)ethylene backbone, involving C–N  $\pi$ -antibonding and C–C  $\pi$ -bonding characters, with small contributions of the carbene and copper centers (Figure 2e). The DFT-computed hyperfine coupling (hfc) constants are consistent with the hfc values obtained from the simulation of the EPR spectrum. The DFT calculation distinguishes two groups in particular for the hydrogen atoms from the NMe<sub>2</sub> groups, depending on whether they are localized on the inner or outer methyl groups, and gives two distinct hfc coupling constants of  $a_H = 22.3$  MHz and  $a_H = 18.9$  MHz. Eventually, the mono-oxidized complex  $[2]^+$  is shown to be stable in solution for 2–3 h at room temperature.

We then tried to generate the di-oxidized complex  $[2]^{2+}$ . Due to the high potential observed for the second oxidation wave in CV ( $E_{1/2} = +1.11$  V vs. SCE), strong oxidizing agents were employed. Thus, complex **2** was reacted at a low temperature ( $-50^\circ\text{C}$ ) with 2.5 equivalents of  $[N(p\text{-BrPh})_3](\text{SbF}_6)$  (Magic Blue,  $E_{1/2} = +1.16$  V vs. SCE) or  $[\text{NO}](\text{SbF}_6)$  ( $E_{1/2} = +1.46$  V vs. SCE), but only mixtures of unidentified products were detected by NMR, and even if the reaction mixture was indeed diamagnetic, no definite conclusion could be drawn on the nature of  $[2]^{2+}$ .

Overall, this first study confirms that NHC ligand **1** behaves as a redox-active ligand in organometallic complexes, and that the mono-oxidized complex  $[2]^+$  is generated and characterized by EPR spectroscopy.

## 2.2. Redox Properties of $\text{IMes}^{(NMe_2)_2}$ Dicarboxyl Rhodium(I) Complex **3**

We then turned our attention to the rhodium carbonyl complex  $[\text{RhCl}(\text{CO})_2(\mathbf{1})]$  (**3**) that we had previously synthesized [36], with the aim of evaluating the overall donor properties of the NHC by means of IR spectroscopy [11].

The cyclic voltammogram of complex **3** displays a first reversible oxidation wave at  $E_{1/2} = +0.71$  V vs. SCE, and a second irreversible oxidation process at  $E_{pa} = +1.26$  V vs. SCE (Figure 3b), whose reversibility may be restored at higher scan rate ( $10 \text{ V} \cdot \text{s}^{-1}$ ). Interestingly, the first oxidation wave of **3** occurs at the same potential as for complex **2**, and, hence, corresponds to an oxidation of the NHC backbone. To confirm the nature of the mono-oxidized state  $[\mathbf{3}]^+$ , we then carried out the chemical oxidation of **3** using one equivalent of 1,1'-diacetylferrocenium tetrafluoroborate in  $\text{CH}_2\text{Cl}_2$  at  $-20^\circ\text{C}$  (Figure 3a), and analyzed  $[\mathbf{3}]^+$  by EPR spectroscopy in  $\text{CH}_2\text{Cl}_2$ /toluene solution (1:1) at room temperature. Unlike the Cu(I) compound  $[2]^+$ , the Rh(I) complex  $[\mathbf{3}]^+$  is stable under these conditions only for several minutes. Analogously to  $[2]^+$ , the EPR spectrum of  $[\mathbf{3}]^+$  features a symmetrical hyperfine coupling pattern (Figure 3c), which is perfectly simulated, taking into account hyperfine interactions between the single electron and the twelve hydrogen atoms of the NMe<sub>2</sub> groups ( $a_H = 18.8$  MHz) and with the two exocyclic nitrogen atoms ( $a_N = 15.6$  MHz). These values are very close to those calculated for  $[2]^+$ , and are corroborated by DFT calculations, which give similar hfc values for those interactions. In addition, the DFT calculations indicate two much smaller hyperfine couplings with the two endocyclic nitrogen atoms and with the  $^{103}\text{Rh}$  center ( $I = \frac{1}{2}$ ), which were not resolved in the experimental spectrum. The experimental and simulated EPR spectra and the computed SOMO orbital in  $[\mathbf{3}]^+$  (Figure 3d) are, thus, in agreement with an organic radical delocalized on the bis(dimethylamino)ethylene backbone of the NHC ligand  $\text{IMes}^{(NMe_2)_2}$ , leaving the Rh(I) center untouched, as already observed for the thiourea  $A^{(NMe_2)_2}$  and the Cu(I) complex **2**. Therefore, it is possible to quantify the effect of the mono-oxidation of the  $\text{IMes}^{(NMe_2)_2}$  ligand on its electronic properties by recording the IR spectra of complexes **3** and  $[\mathbf{3}]^+$ , as the average frequency of the two  $\nu_{\text{CO}}$  bands in the complexes  $[\text{RhCl}(\text{CO})_2(\text{NHC})]$  in  $\text{CH}_2\text{Cl}_2$  is linearly correlated to the Tolman electronic parameter (TEP) value of the NHC ligand [45,46]. While the carbonyl stretching in **3**

are measured at 1992 and 2075  $\text{cm}^{-1}$  (TEP = 2047  $\text{cm}^{-1}$ ), the two bands shift to higher frequencies upon oxidation to  $[3]^+$  and are observed at 2010 and 2090  $\text{cm}^{-1}$  (TEP = 2060  $\text{cm}^{-1}$ ).

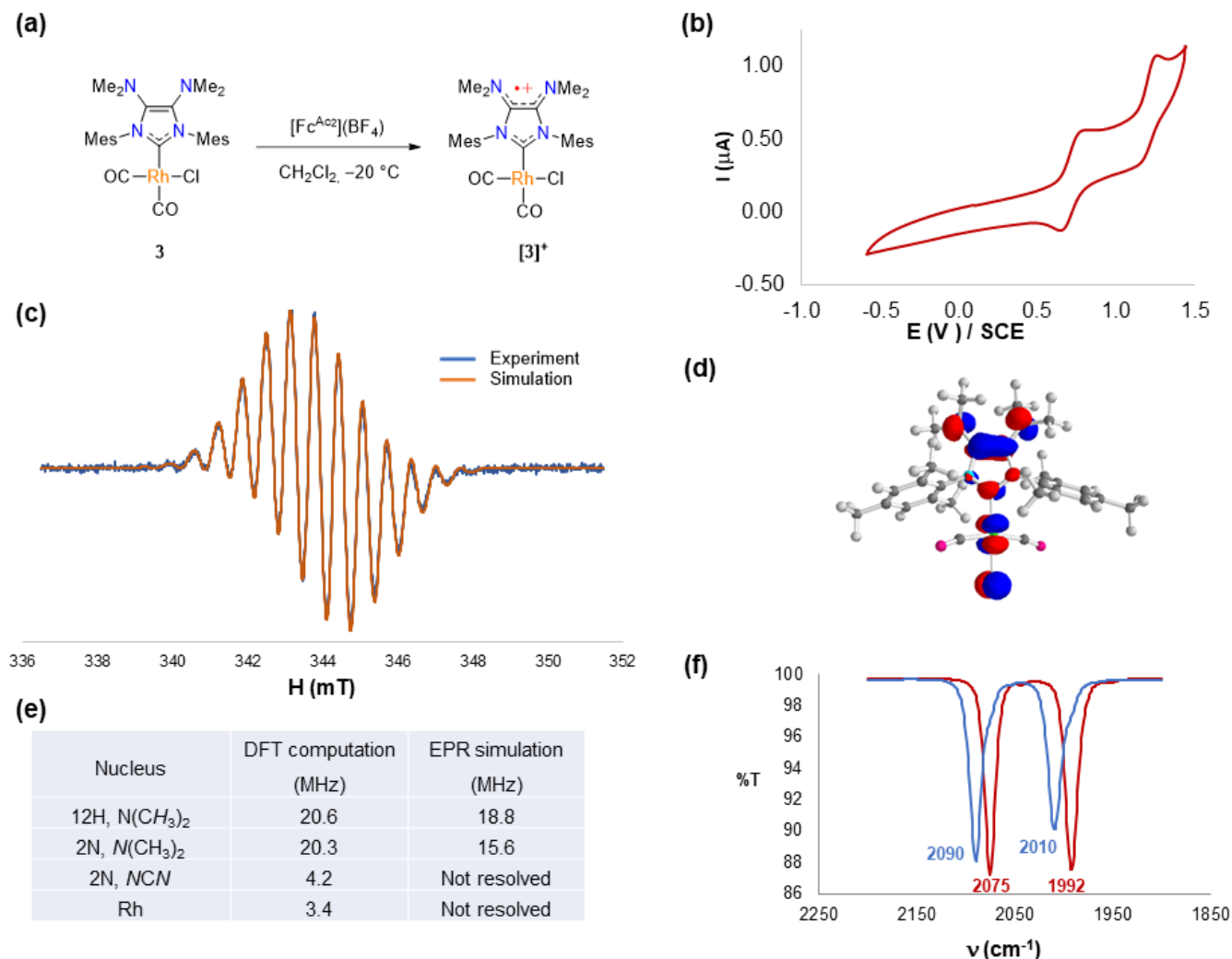


**Figure 3.** (a) Chemical oxidation of complex **3** into  $[3]^+$ . (b) Cyclic voltammogram of complex **3** (Pt working electrode, 1 mM in  $\text{CH}_2\text{Cl}_2$  with 0.1 M  $\text{Bu}_4\text{NPF}_6$  as the supporting electrolyte, 200  $\text{mV} \cdot \text{s}^{-1}$  scan rate; potentials are calibrated against  $\text{Fc}/\text{Fc}^+$  as internal standard with  $E_{1/2}(\text{Fc}/\text{Fc}^+) = +0.46$  V vs. SCE). (c) X-band EPR spectrum of  $[3]^+$  in  $\text{CH}_2\text{Cl}_2$ /toluene solution (1:1) at room temperature: microwave frequency = 9.65225 GHz, mod. ampl. = 0.05 mT, power = 5 mW. Simulation parameters:  $g_{\text{iso}} = 2.00354$ ,  $lw = 0.4$  mT (Gaussian). (d) DFT-optimized structure of  $[3]^+$ , and representation of the SOMO (isodensity value of 0.05 a.u.). (e) Isotropic hyperfine coupling constants obtained by DFT computation and by simulation. (f) IR spectra of complexes **3** (in red) and  $[3]^+$  (in blue) in 2250–1850  $\text{cm}^{-1}$  range in  $\text{CH}_2\text{Cl}_2$  solution.

A scale of TEP values of selected, relevant NHC ligands is depicted in Figure 4. While the ligand  $\text{IMes}^{(\text{NMe}_2)_2}$  is a better donor than the regular IMes, the mono-oxidized cationic radical  $[\text{IMes}^{(\text{NMe}_2)_2}]^{\bullet+}$  is a quite weak electron-donor, and is an even weaker donor than the naphthoquinone-annelated  $\text{IMes}^{\text{N}^{\text{Q}}}$  (TEP = 2056.6  $\text{cm}^{-1}$ ) [22,47], the (amino)(amido)carbene  $\text{SIMes}^{=\text{O}}$  (TEP = 2058  $\text{cm}^{-1}$ ) [48], and the cationic  $\text{IMes}^{(\text{NMe}_3)^+}$  (TEP = 2055.7  $\text{cm}^{-1}$ ) [49]. However, it remains a greater donor than the least electron-donating NHC ligands represented by the diamidocarbene  $\text{SIMes}^{(=\text{O})_2}$  (TEP = 2068  $\text{cm}^{-1}$ ) [50], the cationic NHC **B** (TEP = 2067  $\text{cm}^{-1}$ ) [51], or the dicyano-substituted NHC **C** (TEP = 2067  $\text{cm}^{-1}$ ) [52]. Interestingly, the difference in TEP values of 13  $\text{cm}^{-1}$  between the two redox states of  $\text{IMes}^{(\text{NMe}_2)_2}$

indicates that the latter constitutes a new class of redox-switchable NHC ligand, with the previous examples relying mainly on the incorporation of redox-active ferrocene-derived moiety, or of a naphthoquinone, into the NHC skeleton [7,53]. Moreover, the relatively high shift between the two oxidation states  $\text{IMes}^{(\text{NMe}_2)_2} / [\text{IMes}^{(\text{NMe}_2)_2}]^{\bullet+}$  can be explained by the fact that the redox event in  $\text{IMes}^{(\text{NMe}_2)_2}$  occurs directly onto the carbenic heterocycle and, thus, has a strong effect on the electron-donating properties of the carbenic center.

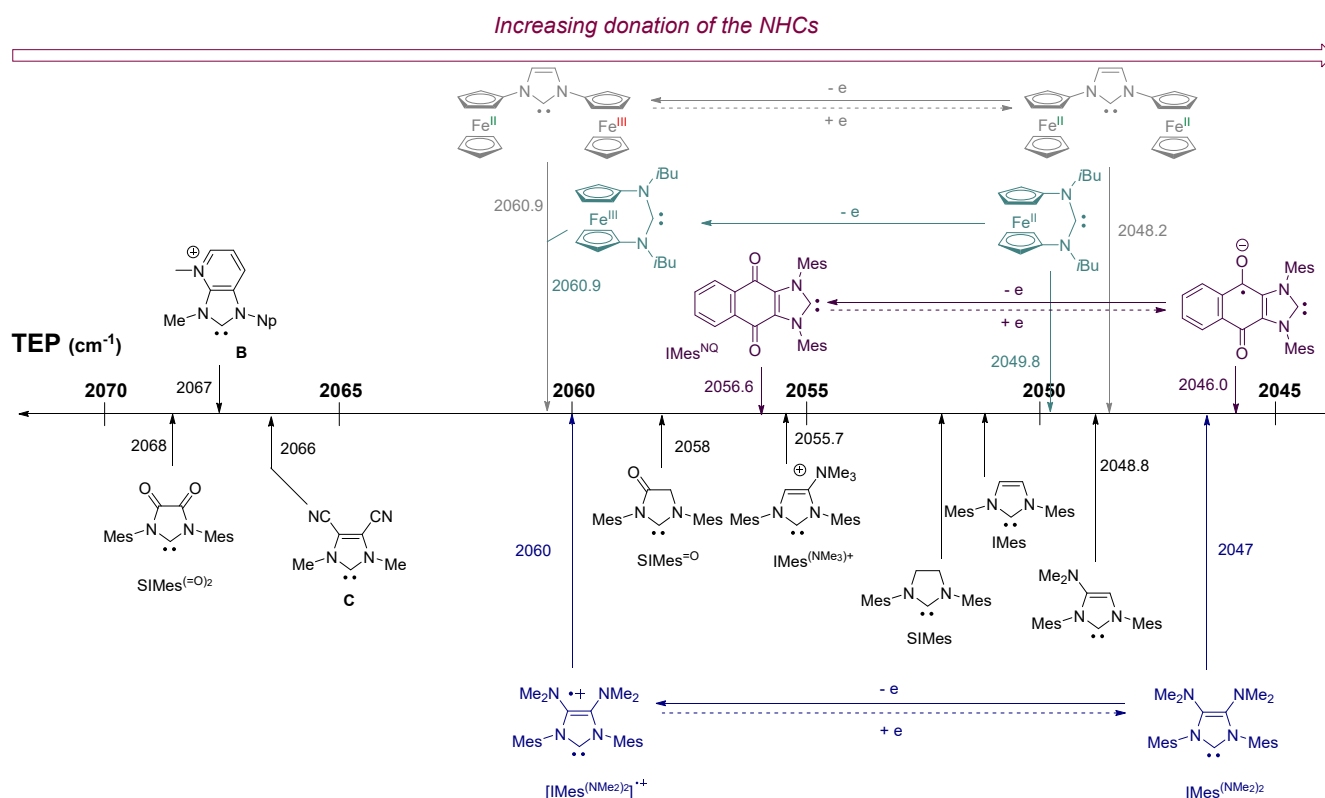
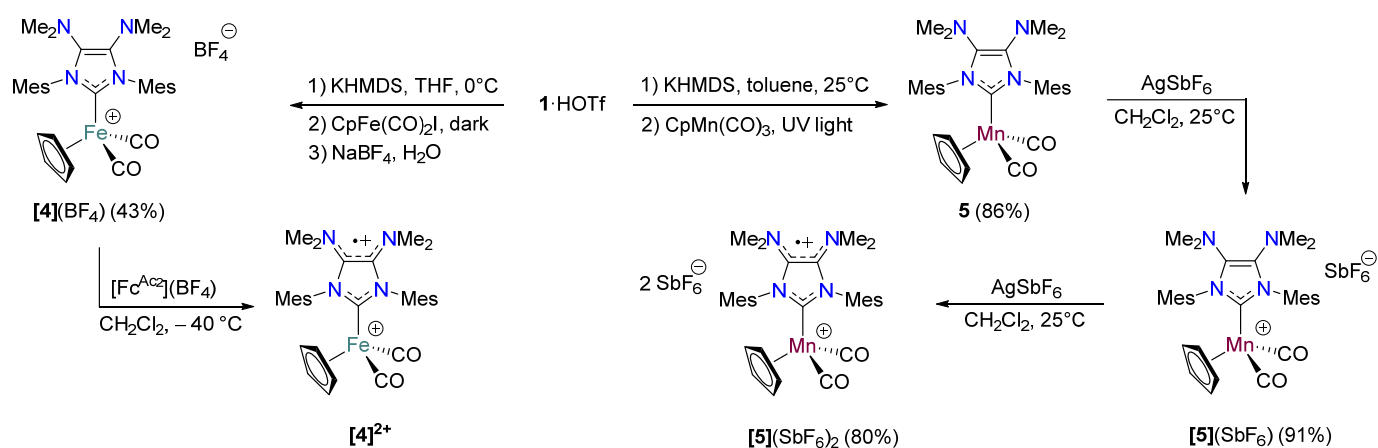


**Figure 4.** TEP value scale of selected, relevant NHCs.

### 2.3. Redox Properties of Half-Sandwich $\text{IMes}^{(\text{NMe}_2)_2}$ Fe(II) and Mn(I) Complexes **[4](BF<sub>4</sub>)** and **5**

The study continued with the two isoelectronic  $d^6$ , 18e<sup>-</sup> valence electron half-sandwich complexes  $[\text{CpFe}(\text{CO})_2(\mathbf{1})](\text{BF}_4)$  (**[4](BF<sub>4</sub>)**), and  $[\text{CpMn}(\text{CO})_2(\mathbf{1})]$  (**5**) of Fe(II), and Mn(I), respectively. Complex **[4](BF<sub>4</sub>)** was synthesized through a slight modification of the synthetic procedure reported by Guerchais for  $[\text{CpFe}(\text{CO})_2(\text{IMes})]\text{I}$  [54]. The free stable carbene **1** was first reacted with the precursor  $[\text{CpFe}(\text{CO})_2\text{I}]$  in the dark to generate the intermediate  $[\text{CpFe}(\text{CO})_2(\mathbf{1})]\text{I}$ , and the iodide anion was then exchanged in situ for the non-coordinating tetrafluoroborate anion  $\text{BF}_4^-$ , to yield the complex **[4](BF<sub>4</sub>)** in 43% isolated yield (Scheme 1). It is of note that the anion metathesis is found to be crucial for the photostability of complex **[4](BF<sub>4</sub>)**. The Mn(I) complex  $[\text{CpMn}(\text{CO})_2(\mathbf{1})]$  (**5**) was synthesized according to a classical UV light-induced substitution of one carbonyl by the free carbene **1** from cymantrene  $[\text{CpMn}(\text{CO})_3]$  [55], and was isolated in very good yield. Both complexes were fully characterized by spectroscopic and analytical methods, and their molecular structures firmly established by single-crystal X-ray diffraction analysis (Figure 5). Beyond the expected piano-stool coordination geometries around the metal and the metal– $\text{C}_{\text{NHC}}$  bond lengths, which are within the classical range for such complexes [54,55], the  $\text{C}4-\text{C}5$  bond lengths are characteristic of a double  $\text{C}=\text{C}$  bond (1.35 Å) [56], and the pyramidalization of the two exocyclic nitrogen atoms ( $\Sigma_{\text{N}} \sim 350^\circ$ ) indicates that the nitrogen lone pairs do not interact with the  $\pi$ -system of the carbenic heterocycle, as previously observed in other complexes [36,39,40].



**Scheme 1.** Synthesis of the Fe(II) complex **[4](BF<sub>4</sub>)**, and chemical generation of the oxidized Fe(II) complex **[4]<sup>2+</sup>** (left). Synthesis of Mn(I) complex **5**, and its stepwise oxidation to Mn(II) derivatives **[5](SbF<sub>6</sub>)** and **[5](SbF<sub>6</sub>)<sub>2</sub>** (right).

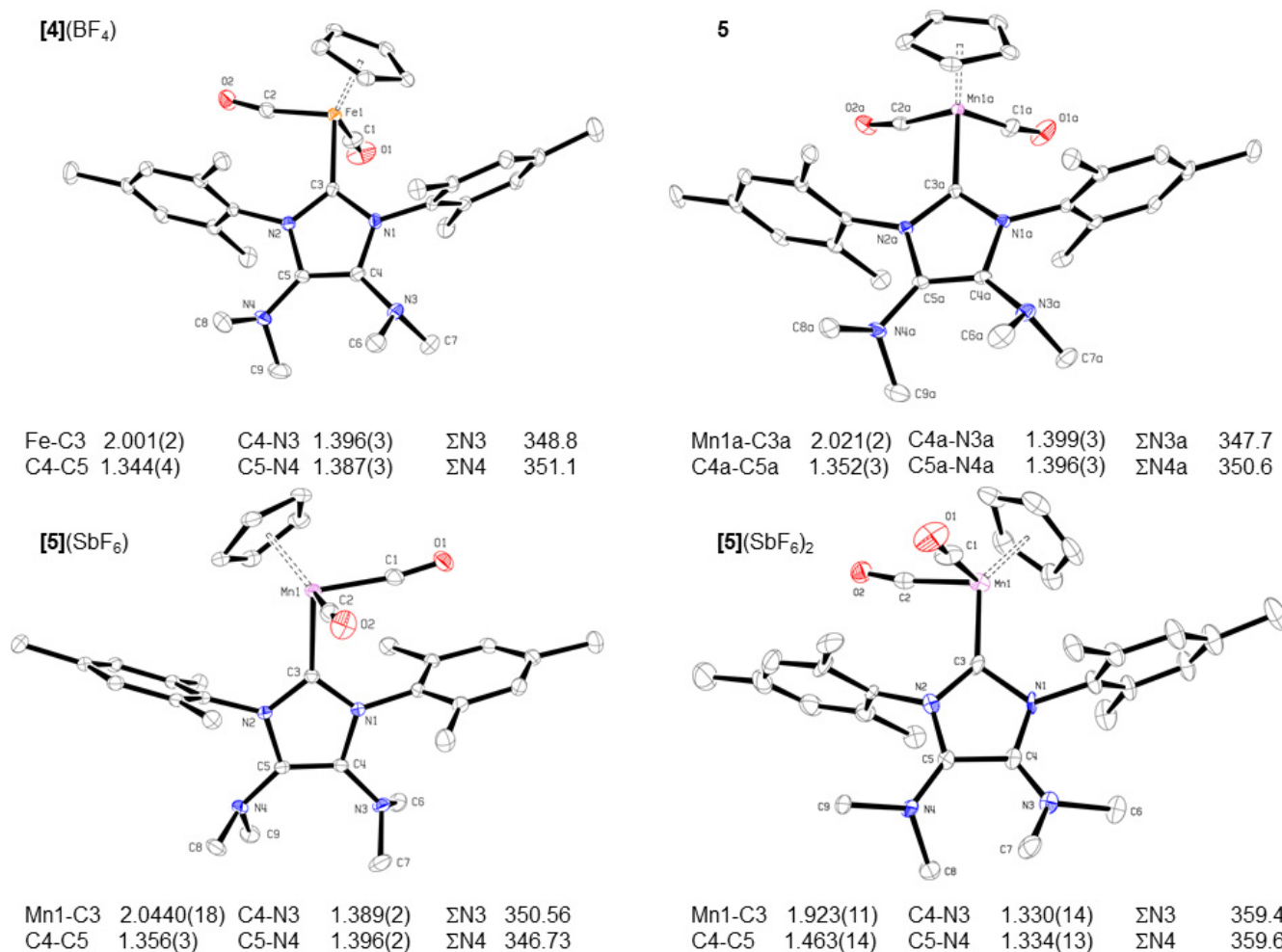


**Figure 5.** Molecular structures of half-sandwich complexes **[4](BF<sub>4</sub>)**, **5**, **[5](SbF<sub>6</sub>)**, and **[5](SbF<sub>6</sub>)<sub>2</sub>**, and selected bond lengths (Å) and angles (deg). Ellipsoids drawn at 30% probability level. Hydrogen atoms and counter-anions omitted for clarity.

While complexes **[4](BF<sub>4</sub>)** and **5** are isoelectronic, their cyclic voltammograms differ substantially (Figure 6). The iron complex **[4](BF<sub>4</sub>)** shows a similar electrochemical behavior

to those of previously studied derivatives **2** and **3**, with a reversible oxidation wave at  $E_{1/2} = +0.84$  V vs. SCE, and an irreversible second oxidation process at  $E_{pa} = +1.36$  V vs. SCE, which indicates that the NHC ligand **1** is still the location where the redox process takes place. Conversely, the much more electron-rich Mn(I) complex **5** exhibits three oxidation processes at  $E_{1/2} = +0.08$  V,  $+0.75$  V, and  $+1.33$  V vs. SCE, with the two first being fully reversible and the latter only partially. The potential at  $+0.08$  V vs. SCE of the first additional oxidation wave lies in the typical range of potentials for the oxidation of Mn(I) to Mn(II) centers in a series of  $[\text{CpMn}(\text{CO})_2(\text{NHC})]$  reported by us [57,58] and others [59], and, thus, corresponds to a metal-centered oxidation process. The lower potential of this process for **5** ( $E_{1/2} = +0.08$  V vs. SCE), compared to the process for the parent  $[\text{CpMn}(\text{CO})_2(\text{IMes})]$  ( $E_{1/2} = +0.16$  V vs. SCE), is also consistent with the more electron-donating character of ligand **1**, relative to the IMes ligand.

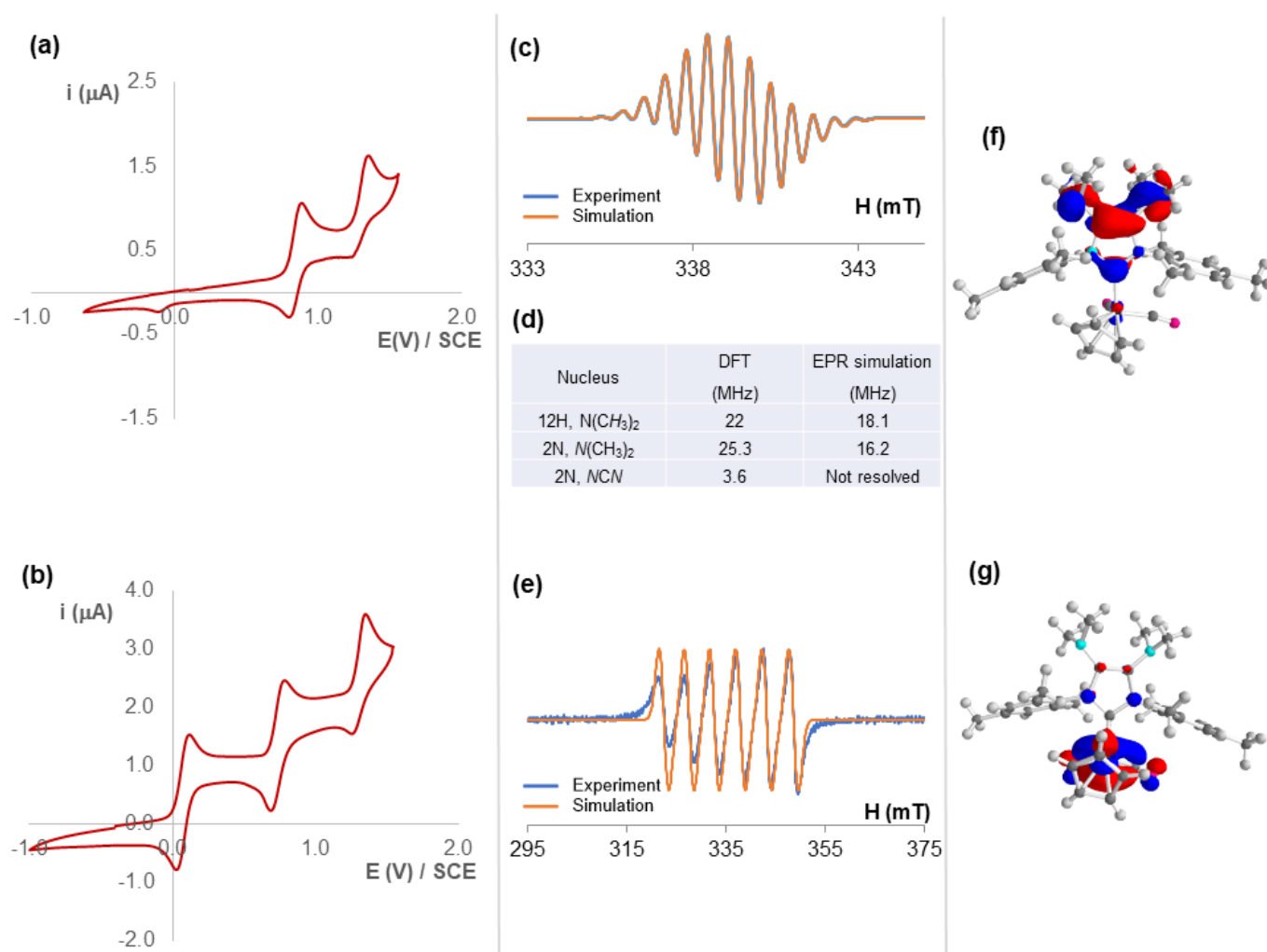


**Figure 6.** (a,b) Cyclic voltammograms of complexes **4** and **5**, respectively (Pt working electrode, 1 mM in  $\text{CH}_2\text{Cl}_2$  with 0.1 M  $\text{Bu}_4\text{NPF}_6$  as the supporting electrolyte,  $200 \text{ mV} \cdot \text{s}^{-1}$  scan rate; potentials are calibrated against  $\text{Fc}/\text{Fc}^+$  as internal standard with  $E_{1/2}(\text{Fc}/\text{Fc}^+) = +0.46$  V vs. SCE). (c) X-band EPR spectrum of  $[\mathbf{4}]^{2+}$  in  $\text{CH}_2\text{Cl}_2/\text{toluene}$  solution (1:1) at room temperature: microwave frequency = 9.5042 GHz, mod. ampl. = 0.1 mT, power = 5 mW. Simulation parameters:  $g_{\text{iso}} = 2.0006$ ,  $lw = 0.43$  mT (Gaussian) (d) Isotropic hyperfine coupling constants obtained by DFT computation and by simulation for  $[\mathbf{4}]^{2+}$ . (e) X-band EPR spectrum of  $[\mathbf{5}]^+$  in  $\text{CH}_2\text{Cl}_2/\text{toluene}$  solution (1:1) at room temperature: microwave frequency = 9.6513 GHz, mod. ampl. = 0.5 mT, power = 2 mW. Simulation parameters:  $g_{\text{iso}} = 2.0537$ ,  $a_{\text{Mn}} = 150.2$  MHz, and  $lw = 1.98$  mT (Gaussian). (f,g) DFT-optimized structures for  $[\mathbf{4}]^{2+}$  and  $[\mathbf{5}]^+$ , respectively, and representation of SOMO (isodensity value of 0.05 a.u.).



These first assumptions are confirmed by the study of the mono-oxidized species  $[4]^{2+}$  and  $[5]^+$ . The Fe-complex  $[4]^{2+}$  is generated chemically by oxidation with 1,1'-diacetylferrocenium tetrafluoroborate, and the resulting red/purple solution analyzed by X-band EPR and IR spectroscopies at room temperature (Figure 6). The same hyperfine coupling pattern is observed as encountered for the previous complexes  $[2]^+$  and  $[3]^+$ , and is perfectly fitted by hyperfine couplings with the 12 hydrogen atoms ( $a_H = 18.1$  MHz) and the two nitrogen atoms ( $a_N = 16.2$  MHz) of the exocyclic NMe<sub>2</sub> groups. IR monitoring of  $[4](BF_4)$  oxidation in CH<sub>2</sub>Cl<sub>2</sub> shows the partial formation of new species  $[4]^{2+}$ , evidenced by the appearance of  $\nu_{CO}$  bands at 2054 and 2015 cm<sup>-1</sup>, which gradually decompose at room temperature, precluding its isolation. The average  $\nu_{CO}$  value for  $[4]^{2+}$  exhibits a ~12 cm<sup>-1</sup> higher frequency shift relative to that of the starting product, thus, showing similar behavior as observed in case of Rh(I) complexes  $3/[3]^+$  (*vide supra*). The calculated SOMO of  $[4]^{2+}$  is also in agreement with the experimental data, and confirms that the radical is mainly localized on the bis(dimethylamino)ethene backbone of ligand **1**. The Mn(I) complex **5** is readily oxidized using one equivalent of AgSbF<sub>6</sub> to yield the oxidized complex  $[5](SbF_6)$ , which is isolated in pure form in 91% yield as black crystals. The X-band EPR spectrum of  $[5]^+$  recorded at room temperature is consistent with a Mn(II) metal center, as the Landé factor of  $g_{iso} = 2.0537$  deviates significantly from an organic radical, and the spectrum is composed of only six equidistant peaks arising from the hyperfine coupling between the unpaired electron and the <sup>55</sup>Mn nucleus ( $I = 5/2$ , abundance = 100%,  $a_{Mn} = 150.2$  MHz). This Mn(I)-to-Mn(II) transformation in  $[5](SbF_6)$  is also confirmed by IR (Figure S2), UV-vis (Figure S3), and paramagnetic <sup>1</sup>H NMR spectroscopy, exhibiting similar features to the previously observed  $[Cp(CO)_2Mn(IMes)](BF_4)$  analogue [54], as well as by an X-ray diffraction analysis of single crystals (Figure 4). Finally, DFT calculations of  $[5]^+$  show that the SOMO is mainly located on the Mn center. In particular, the molecular structure of  $[5](SbF_6)$  shows that the metrics within the NHC ligand **1** remain about the same compared to the non-oxidized complex **5**, especially on the diaminoethene backbone. As expected for such Mn(II) NHC complexes, the Mn1–C3 bond [2.0440(18) Å] (DFT *in vacuo*: 2.015 Å) is a little elongated, relative to the Mn1–C3a bond in **5** [2.021(2) Å] [57].

The full reversibility of the second oxidation wave in the CV of **5** then prompted us to explore the oxidation of  $[5](SbF_6)$ . The latter is cleanly oxidized by using one more equivalent of AgSbF<sub>6</sub> in CH<sub>2</sub>Cl<sub>2</sub> to give a dark blue solution, from which the dicationic complex  $[5](SbF_6)_2$  is isolated as a black powder in 80% yield. In contrast to the first metal-centered oxidation of complex **5**, leading to ca. 120 cm<sup>-1</sup> high frequency shift of  $\nu_{CO}$  bands, the average stretching CO frequencies are much less affected upon the  $[5]^+ \rightarrow [5]^{2+}$  transformation (+7.5 cm<sup>-1</sup>), being consistent with the occurrence of electron transfer at the NHC ligand. The intense absorption at 578 nm observed in the UV-vis spectrum of  $[5](SbF_6)_2$  (Figure S3) is similar to that observed for the radical cation of  $[A^{(NMe_2)_2}]^+$  (590 nm), previously attributed to the electronic transition involving SOMO orbital by TD-DFT calculations [32]. Important changes are worth mentioning in the molecular structure of  $[5](SbF_6)_2$  as compared to  $[5](SbF_6)$  and **5** (Figure 5), especially on the NHC backbone. Indeed, the two exocyclic nitrogen atoms are no longer pyramidalized but planar [ $\Sigma_{N3} = 359.4^\circ$ ,  $\Sigma_{N4} = 359.6^\circ$ ], the C4–C5 bond of the imidazolyl ring is elongated [+0.11 Å] relative to C4–C5 bonds in **5** and  $[5]^+$ , and the C4–N3 and C5–N4 bonds are shortened [ca. -0.06 Å] relative to the corresponding bonds in **5** and  $[5]^+$ . This is consistent with a  $\pi$ -delocalization through the bis(dimethylamino)ethene backbone N3–C4–C5–N4 of a radical cation, as already calculated in the previous complexes. Moreover, the strong shortening of the Mn1–C3 bond [1.923(11) Å] in  $[5]^{2+}$  relative to 2.0440(18) Å in  $[5]^+$ , is consistent with an enhanced  $\pi$ -backbonding from the Mn center into the more  $\pi$ -acidic, oxidized ligand  $1^{\bullet+}$ . It is of note that this example represents the shortest Mn–NHC bond reported in the literature, being comparable only with two Mn(I) and Mn(IV) complexes bearing pincer (1.9360(16) Å [60] and tripod (1.938(2) Å [61] imidazol-2-ylidene ligands, respectively. From a magnetic point of view, both the triplet state ( $S = 1$ ) and broken symmetry state ( $M_s = 0$ ) are quasi-isoenergetic (i.e., within DFT error, a few tens of cm<sup>-1</sup>).

This does not allow us to conclude what the spin ground state of  $[5]^{2+}$  ( $S = 1$  or  $S = 0$ ), and what is expected to be observed by EPR.

As it turns out, no signal is detected by recording the EPR spectra of complex  $[5](SbF_6)_2$  at various temperatures (from 4.2 K to room temperature). DFT only predicted that the two single electrons are expected to be weakly magnetically coupled. The fact that no EPR signal is observed could be due to a relatively high zero-field splitting constant of the EPR spectrum of the  $S = 1$  (typically  $D > 1 \text{ cm}^{-1}$ ), possibly associated with very short relaxation times. These features would lead either to low-field (X-band) EPR silent  $S = 1$  system ( $D > 1 \text{ cm}^{-1}$ ) [62], or to a very broad EPR signal (very short relaxation times) [63], which is lower in intensity than the detection limit of our EPR spectrometer.

### 3. Materials and Methods

All manipulations were performed under an inert atmosphere of dry nitrogen by using standard vacuum line and Schlenk tube techniques. Glassware was dried at  $120^\circ\text{C}$  in an oven, for at least three hours. THF, diethyl ether, pentane, toluene, and  $\text{CH}_2\text{Cl}_2$  were dried using an innovative technology solvent purification system.

Imidazolium triflate  $\text{IMes}^{(\text{NMe}_2)_2}\cdot\text{HOTf}$  (**1**·HOTf) [36],  $[\text{RhCl}(\text{CO})_2(\text{IMes}^{(\text{NMe}_2)_2})]$  [36], and  $[\text{CpFe}(\text{CO})_2\text{I}]$  [64] were prepared according to procedures in the literature. Following one such procedure, 1,1'-diacetylferrocenium tetrafluoroborate was prepared through the oxidation of 1,1'-diacetylferrocene by benzoquinone/ $\text{HBF}_4\cdot\text{OEt}_2$  [65].  $\text{CuCl}$  was purified by dissolution in the minimum of concentrated  $\text{HCl}$ , followed by precipitation by adding distilled water, and filtration through a fritted funnel. The off-white powder was dried carefully and stored in a glovebox. Technical quality  $[\text{CpMn}(\text{CO})_3]$  was purified by the crystallization from hexane, as described earlier [66]. The 0.5 M solution of KHMDS in toluene was prepared by weighing 2.0 g of solid KHMDS (stored in a glovebox) in a volumetric flask, and adding toluene to complete to 20 mL.  $\text{AgSbF}_6$  (Aldrich) was stored in the glovebox. All other reagents were commercially available, and used as received.

NMR spectra were recorded on Bruker AV300 or AV400 spectrometers. Chemical shifts are reported in ppm ( $\delta$ ) compared to TMS ( $^1\text{H}$  and  $^{13}\text{C}$ ), using the residual peak of deuterated solvent as internal standard [67]. Solution IR spectra were recorded in 0.1 mm  $\text{CaF}_2$  cells using a PerkinElmer Frontier FT-IR spectrometer, and given in  $\text{cm}^{-1}$  with relative intensities in parentheses. UV-vis spectra were recorded on a Perkin Elmer Lambda 950 UV/Vis/NIR spectrometer in 1 cm quartz cell under nitrogen atmosphere ( $\text{CH}_2\text{Cl}_2$ ,  $10^{-4}$  M sample concentration). Elemental analyses were performed by the microanalytical service of the LCC, and mass spectra (ESI mode) by the mass spectrometry service of the "Institut de Chimie de Toulouse".

X-band EPR data were recorded using Elexsys ESP 500 and EMX Bruker EPR spectrometers. Typical settings: 2 mW microwave power and 0.1 mT modulation amplitude. For all species, spectra recorded with lower modulation amplitudes do not reveal more lines or different patterns (data not shown). Landé factors were measured by comparison with a reference DPPH sample ( $g = 2.0036$ ). The numerical simulation of EPR spectra was performed using EasySpin software [68].

#### Chloro-(1,3-dimesityl-4,5-bis(dimethylamino)imidazol-2-ylidene)copper(I) (**2**).

A solution of KHMDS (0.5 M in toluene, 610  $\mu\text{L}$ , 0.31 mmol, 1.1 equiv) was added dropwise to a solution of **1**·HOTf (150 mg, 0.278 mmol) in THF (15 mL), at  $0^\circ\text{C}$ . After 10 min,  $\text{CuCl}$  (55 mg, 0.56 mmol, 2 equiv.) was added as a solid, followed by  $\text{NaCl}$  (97.3 mg, 1.66 mmol, 6 equiv.), and the solution was stirred at room temperature for 1.5 h. After the evaporation of THF, the crude product was dissolved in toluene, and filtered over Celite. The toluene was evaporated, and the resulting brownish solid was washed with pentane, to afford complex **2** (133 mg, 96%) as a white powder.

$^1\text{H}$  NMR (400 MHz,  $\text{CDCl}_3$ ):  $\delta = 6.96$  (s, 4H,  $\text{CH}_{\text{Mes}}$ ), 2.58 (s, 12H,  $\text{N}-\text{CH}_3$ ), 2.33 (s, 6H,  $\text{CH}_3_{\text{para}}$ ), 2.12 (s, 12H,  $\text{CH}_3_{\text{ortho}}$ ).

$^{13}\text{C}\{^1\text{H}\}$  NMR (101 MHz,  $\text{CDCl}_3$ ):  $\delta = 171.8$  ( $\text{N}_2\text{C}-\text{Cu}$ ), 138.9, 135.2, 134.3, 133.9 ( $\text{C}_{\text{Ar}}$ ), 129.5 ( $\text{CH}_{\text{Mes}}$ ), 43.3 ( $\text{N}-\text{CH}_3$ ), 21.3 ( $\text{CH}_3_{\text{para}}$ ), 18.3 ( $\text{CH}_3_{\text{ortho}}$ ).

MS (ESI, positive mode):  $m/z$  (%): 494 (100)  $[M-Cl + MeCN]^+$ .

HRMS (ESI):  $m/z$  calcd. for  $C_{27}H_{37}N_5^{63}Cu^+$ : 494.2345, found 494.2354,  $\epsilon_r = 1.8$  ppm.

#### Generation and EPR characterization of $[2]^+$

Solid 1,1'-diacetylferrocenium tetrafluoroborate (4.2 mg, 12  $\mu$ mol, 1.0 equiv.) was added to a solution of complex **2** (5.8 mg, 12  $\mu$ mol, 1.0 equiv.) in  $CH_2Cl_2$  (1 mL) at  $-40$  °C. After 5 min, 50  $\mu$ L of the reaction mixture was syringed in an EPR tube at room temperature, which was completed with 50  $\mu$ L of toluene. The EPR spectrum was immediately recorded. Compound  $[2]^+$  was stable for at least 3 h at room temperature.

#### Generation and EPR characterization of $[3]^+$

Solid 1,1'-diacetylferricinium tetrafluoroborate (4.3 mg, 12  $\mu$ mol, 1.0 equiv.) was added to a solution of complex **3** (7.0 mg, 12  $\mu$ mol, 1.0 equiv.) in  $CH_2Cl_2$  (1 mL), at  $-20$  °C. The solution became violet. After 5 min, 50  $\mu$ L of the reaction mixture was syringed in an EPR tube at room temperature, which was completed with 50  $\mu$ L of toluene. The EPR spectrum was immediately recorded.

#### $(\eta^5\text{-Cyclopentadienyl})\text{-Dicarbonyl-(1,3-Dimesityl-4,5-Bis(Dimethylamino)Imidazol-2-ylidene)iron (II) Tetrafluoroborate [4](BF}_4\text{)}$

A solution of KHMDS (0.5 M in toluene, 380  $\mu$ L, 0.19 mmol, 1.02 equiv.) was added dropwise to a solution of **1**·HOTf (100 mg, 0.185 mmol) in toluene (5 mL), at 0 °C. After 30 min, the toluene was evaporated, in order to remove HMDS, and the crude product was dissolved anew in 5 mL toluene, and filtered over Celite under nitrogen. The toluene was evaporated, and the carbene was dissolved in dry THF (5 mL).  $CpFe(CO)_2I$  (61.8 mg, 0.2 mmol, 1.08 equiv.) was added as a solid in the dark (under visible light irradiation, a carbonyl ligand can be removed and replaced by the iodine counter-anion). The solution was stirred for 1 h at room temperature, and THF was evaporated (always in the absence of light). The solid was taken up in dichloromethane (5 mL), degassed water (5 mL) and  $NaBF_4$  (61.5 mg, 0.56 mmol, 3 equiv.) were added, and the reaction mixture was stirred for 30 min. The organic phase was isolated, dried over  $Na_2SO_4$ , and evaporated. The yellow solid was eventually washed with ether, and crystallized by the slow diffusion of a dichloromethane solution in diethyl ether, to afford **[4](BF<sub>4</sub>)** (67 mg, 54%) as yellow crystals, some of which were suitable for X-ray diffraction.

$^1H$  NMR (400 MHz,  $CDCl_3$ ):  $\delta = 7.07$  (s, 4H,  $CH_{Mes}$ ), 4.73 (s, 5H,  $CH_{Cp}$ ), 2.54 (s, 12H,  $NCH_3$ ), 2.39 (s, 6H,  $CH_3_{para}$ ), 2.09 (s, 12H,  $CH_3_{ortho}$ ).

$^{13}C\{^1H\}$  NMR (101 MHz,  $CDCl_3$ ):  $\delta = 209.8$  (Fe–CO), 162.7 ( $N_2C-Fe$ ), 140.6, 139.7, 136.3, 134.6 ( $C_{Ar}$ ), 130.0 ( $CH_{Mes}$ ), 86.3 ( $CH_{Cp}$ ), 43.5 ( $N-CH_3$ ), 21.3 ( $CH_3_{para}$ ), 18.7 ( $CH_3_{ortho}$ ).

IR ( $CH_2Cl_2$ )  $\nu_{CO}$  2045 (s), 2001 (s)  $cm^{-1}$ .

MS (ESI, positive mode):  $m/z$  (%): 362 (100)  $[M - BF_4]^+$

HRMS (ESI):  $m/z$  calcd. for  $C_{32}H_{39}N_4O_2^{56}Fe^+$ : 567.2422, found 567.2432,  $\epsilon_r = 1.8$  ppm.

#### Generation and EPR characterization of $[4]^{2+}$

Solid 1,1'-diacetylferrocenium tetrafluoroborate (4.2 mg, 12  $\mu$ mol, 1.0 equiv.) was added to a solution of complex **[4](BF<sub>4</sub>)** (7.8 mg, 12  $\mu$ mol, 1.0 equiv.) in  $CH_2Cl_2$  (1 mL), at  $-20$  °C. After 5 min, 50  $\mu$ L of the reaction mixture was syringed in an EPR tube at room temperature, which was completed with 50  $\mu$ L of toluene. The EPR spectrum was immediately recorded. Compound  $[4]^{2+}$  was stable for at least 3 h at room temperature.

IR ( $CH_2Cl_2$ ):  $\nu_{CO}$  2054 (s), 2015 (s)  $cm^{-1}$ .

#### $(\eta^5\text{-Cyclopentadienyl})\text{-Dicarbonyl-(1,3-Dimesityl-4,5-Bis(Dimethylamino)Imidazol-2-ylidene)Manganese (I) (5)}$

To a suspension of **1**·HOTf (216 mg, 0.4 mmol) in toluene (30 mL), a solution of KHMDS (0.9 mL of 0.5 M, 0.45 mmol, 1.1 equiv.) was added, and the resulting, slightly yellow solution was sonicated for 5 min, and then stirred at RT for 15 min.  $CpMn(CO)_3$  (82 mg, 0.4 mmol, 1 equiv.) was added, and the reaction mixture was irradiated with UV light (370–380 nm), using a custom LED-based reactor (*ca.* 15W power), until  $\nu_{CO}$  bands of the product at the measurements of 1904 and 1831  $cm^{-1}$  ceased to increase (*ca.* 1h). The toluene was evaporated under vacuum, and the residue was purified by column chromatography on silica (1  $\times$  6 cm). A slightly yellow band containing traces of cymantrene was eluted

with 10:1 hexane/toluene mixture, followed by yellow–orange band of the target product. The solution was evaporated under vacuum, and the crude product was crystallized from ether/hexane mixture at  $-20\text{ }^{\circ}\text{C}$ , to afford **5** (195 mg, 86%) as yellow crystals. Single crystals, suitable for X-ray diffraction, were obtained from concentrated solution in toluene at room temperature.

$^1\text{H}$  NMR (400 MHz,  $\text{C}_6\text{D}_6$ ):  $\delta$  = 6.92 (s, 4H,  $\text{CH}_{\text{Mes}}$ ), 4.02 (s, H,  $\text{CH}_{\text{Cp}}$ ), 2.23 (s, 12H,  $\text{NCH}_3$ ), 2.20 (s, 18H,  $\text{CH}_3_{\text{Mes}}$ ).

$^{13}\text{C}\{^1\text{H}\}$  NMR (101 MHz,  $\text{C}_6\text{D}_6$ ):  $\delta$  = 234.7 (Mn–CO), 198.0 ( $\text{N}_2\text{C}$ –Mn), 138.1, 137.2, 137.1, 136.5 ( $\text{C}_{\text{Ar}}$ ), 129.4 ( $\text{CH}_{\text{Mes}}$ ), 81.8 ( $\text{CH}_{\text{Cp}}$ ), 43.4 (N– $\text{CH}_3$ ), 21.2 ( $\text{CH}_3_{\text{para}}$ ), 19.3 ( $\text{CH}_3_{\text{ortho}}$ ).

IR ( $\text{CH}_2\text{Cl}_2$ ):  $\nu_{\text{CO}}$  1904 (s), 1830 (s)  $\text{cm}^{-1}$ .

UV–vis ( $\text{CH}_2\text{Cl}_2$ ):  $\lambda$  387 nm ( $\epsilon$  1400  $\text{M}^{-1}\text{cm}^{-1}$ ).

Elemental analysis: *calcd* (%) for  $\text{C}_{32}\text{H}_{39}\text{MnN}_4\text{O}_2$  (MW = 566.6): C 67.83, H 6.94, N 9.89; *found*: C 68.15, H 7.20, N 9.91.

**( $\eta^5$ -Cyclopentadienyl)-Dicarbonyl-(1,3-dimesityl-4,5-Bis(Dimethylamino)Imidazol-2-Ylidene)Manganese (II) Hexafluoroantimonate ([5](SbF<sub>6</sub>)).**

To a stirred yellow solution of complex **5** (142 mg, 0.25 mmol) in  $\text{CH}_2\text{Cl}_2$  (5 mL), solid  $\text{AgSbF}_6$  (86 mg, 0.25 mmol, 1 equiv.) was added, in one portion, at  $-20\text{ }^{\circ}\text{C}$ . The color of the reaction turned green–brown, and the precipitate of metallic silver gradually appeared. The reaction mixture was warmed to room temperature, and stirred for 15 min. IR analysis of the aliquot shows the quantitative conversion of the starting material, and the appearance of new bands at  $\nu_{\text{CO}}$  2027 and 1950  $\text{cm}^{-1}$ , belonging to the oxidation product [5](SbF<sub>6</sub>). The solvent was evaporated under vacuum; the residue was again dissolved in  $\text{CH}_2\text{Cl}_2$  (2 mL), and filtered through Celite. Diethyl ether (20 mL) was added dropwise to the resulting green–brown solution under vigorous stirring, to induce the precipitation of the product. The supernatant was removed by decantation, and the precipitate was washed with additional  $\text{Et}_2\text{O}$  (5 mL), and dried under vacuum to give [5](SbF<sub>6</sub>) (182 mg, 91%) as black microcrystalline powder. Single crystals, suitable for X-ray diffraction, were obtained by vapor diffusion of ether into a concentrated solution of [5](SbF<sub>6</sub>) in dichloromethane.

$^1\text{H}$  NMR (400 MHz,  $\text{CD}_2\text{Cl}_2$ , 25  $^{\circ}\text{C}$ ):  $\delta$  14.09 (5H,  $w_{\frac{1}{2}} = 1300$  Hz, Mn–Cp), 8.13 (4H,  $w_{\frac{1}{2}} = 70$  Hz,  $\text{CH}_{\text{Mes}}$ ), 6.67 (6H,  $w_{\frac{1}{2}} = 300$  Hz, Me), 5.96 (12H,  $w_{\frac{1}{2}} = 150$  Hz, Me), 2.47 (12H,  $w_{\frac{1}{2}} = 180$  Hz, Me).

IR ( $\text{CH}_2\text{Cl}_2$ ):  $\nu_{\text{CO}}$  2027 (s), 1950 (s),  $\nu_{\text{C=C}}$  1665–1600 (m br)  $\text{cm}^{-1}$ .

UV–vis ( $\text{CH}_2\text{Cl}_2$ ):  $\lambda_1$  434 ( $\epsilon$  1200  $\text{M}^{-1}\text{cm}^{-1}$ ),  $\lambda_1$  662 nm ( $\epsilon$  550  $\text{M}^{-1}\text{cm}^{-1}$ ).

Elemental analysis: *calcd* (%) for  $\text{C}_{32}\text{H}_{39}\text{F}_6\text{MnN}_4\text{O}_2\text{Sb}$  (MW = 802.4): C 47.90, H 4.90, N 6.98; *found*: C 48.17, H 5.09, N 6.64.

**( $\eta^5$ -Cyclopentadienyl)-Dicarbonyl-(1,3-Dimesityl-4,5-Bis(Dimethylamino)Imidazol-2-Ylidene)Manganese (II) (bis)Hexafluoroantimonate ([5](SbF<sub>6</sub>)<sub>2</sub>).**

To a stirred yellow solution of complex [5](SbF<sub>6</sub>) (105 mg, 0.13 mmol) in  $\text{CH}_2\text{Cl}_2$  (5 mL), solid  $\text{AgSbF}_6$  (45 mg, 0.13 mmol, 1 equiv.) was added, in one portion, at  $-20\text{ }^{\circ}\text{C}$ . The color of the reaction mixture immediately changed to deep blue, and black precipitate appeared. The reaction mixture was slowly warmed to room temperature, stirred for additional 30 min, and the volatiles were removed under vacuum. The residue was repeatedly extracted with  $\text{CH}_2\text{Cl}_2$  under sonication (6  $\times$  5 mL), combined dark blue solutions were filtered through Celite, and  $\text{Et}_2\text{O}$  (25 mL) was added dropwise under vigorous stirring, to induce the precipitation of the product. The supernatant was removed by decantation, and the precipitate was washed with ether (10 mL) and dried under vacuum to give [5](SbF<sub>6</sub>)<sub>2</sub> (108 mg, 80%) as deep violet powder. Single crystals, suitable for X-ray diffraction, were obtained by the layering of toluene on the solution of [5](SbF<sub>6</sub>)<sub>2</sub> in  $\text{CH}_2\text{Cl}_2$  at  $-20\text{ }^{\circ}\text{C}$ .

$^1\text{H}$  NMR (400 MHz,  $\text{CD}_2\text{Cl}_2$ , 25  $^{\circ}\text{C}$ ):  $\delta$  8.60 (8H,  $w_{\frac{1}{2}} = 300$  Hz, Mn–Cp + Me), 7.11 (4H,  $w_{\frac{1}{2}} = 35$  Hz,  $\text{CH}_{\text{Mes}}$ ), 5.04 (3H,  $w_{\frac{1}{2}} = 25$  Hz, Me), 2.73–2.05 (several overlapping signals of variable width, 18H, Me), 1.26 (3H,  $w_{\frac{1}{2}} = 13$  Hz, Me), 0.85 (3H,  $w_{\frac{1}{2}} = 30$  Hz, Me).

IR ( $\text{CH}_2\text{Cl}_2$ ):  $\nu_{\text{CO}}$  2024 (s), 1968 (s),  $\nu_{\text{C=C}}$  1602 (s)  $\text{cm}^{-1}$ .

UV–vis ( $\text{CH}_2\text{Cl}_2$ ):  $\lambda_1$  386 ( $\epsilon$  2400  $\text{M}^{-1}\text{cm}^{-1}$ ),  $\lambda_2$  590 nm ( $\epsilon$  8000  $\text{M}^{-1}\text{cm}^{-1}$ ).

Elemental analysis: *calcd* (%) for  $C_{32}H_{39}F_{12}MnN_4O_2Sb_2 \times CH_2Cl_2$  (MW = 1123.1): C 35.29, H 3.68, N 4.99; *found*: C 35.32, H 3.72, N 4.79.

#### Electrochemical studies

Cyclic voltametric measurements were carried out with a Autolab PGSTAT100 potentiostat, controlled by GPES 4.09 software. Experiments were performed under argon at room temperature, in a homemade airtight three-electrode cell. The reference electrode consisted of a saturated calomel electrode (SCE) separated from the solution by a glass frit. The counter electrode was a platinum wire of ca.  $1\text{ cm}^2$  apparent surface. The working electrode was a Pt microdisk (0.5 mm diameter). The supporting electrolyte,  $[nBu_4N](PF_6)$  (99% electrochemical grade), was dried at  $120\text{ }^\circ\text{C}$  and stored under Ar. The  $CH_2Cl_2$  solutions of **2**, **3**, **[4]**( $BF_4$ ), and **5** used for the electrochemical studies were typically  $10^{-3}\text{ M}$  in complex, and  $0.1\text{ M}$  in supporting electrolyte. Before each measurement, the solutions were degassed by bubbling Ar, and the working electrode was polished with a polishing machine. Potentials are referenced to the SCE, and were calibrated using the  $Fc/Fc^+$  couple, by adding ferrocene ( $10^{-3}\text{ M}$ ) at the end of the experiments. Under the experimental conditions employed in this work, the half-wave potential ( $E_{1/2}$ ) of the  $Fc^+/Fc$  couple in  $CH_2Cl_2$  occurs at  $E_{1/2} = +0.46\text{ V}$  vs. SCE. Cyclic voltametric studies include the study of the compounds in oxidation, and in reduction at various scan rates (from  $50\text{ mV/s}$  to  $10\text{ V/s}$ ).

**X-ray diffraction analyses.** X-ray diffraction data were collected on a Bruker SMART / APEX II diffractometer (**[4]**( $BF_4$ )), an Oxford diffraction Gemini diffractometer (**5**), an Xcalibur Gemini Ultra diffractometer (**[5]**( $SbF_6$ )), or on a Bruker D8/APEX II/Incoatec Mo  $I\mu S$  Microsource diffractometer (**[5]**( $SbF_6$ )<sub>2</sub>) using, in most cases,  $MoK\alpha$  radiation ( $\lambda = 0.71073\text{ \AA}$ , graphite monochromator), besides complex **[5]**( $SbF_6$ ), for which  $CuK\alpha$  radiation ( $\lambda = 1.54184\text{ \AA}$ , graphite monochromator) was used. Crystal and structure refinement details are given in the Table S1. All calculations were performed on a PC compatible computer using the WinGX system [69]. The structures were solved using the SIR92 program [70], which revealed in each instance the position of most of the non-hydrogen atoms. All the remaining non-hydrogen atoms were located by the usual combination of full matrix least-squares refinement, and difference electron density syntheses using the SHELX program [71]. Atomic scattering factors were taken from the usual tabulations. Anomalous dispersion terms for the Mn and Fe atoms were included in Fc. All non-hydrogen atoms were allowed to vibrate anisotropically. The hydrogen atoms were set in idealized positions ( $R_3CH$ ,  $C-H = 0.96\text{ \AA}$ ;  $R_2CH_2$ ,  $C-H = 0.97\text{ \AA}$ ;  $RCH_3$ ,  $C-H = 0.98\text{ \AA}$ ;  $C(sp^2)-H = 0.93\text{ \AA}$ ;  $U_{iso}$  1.2 or 1.5 times greater than the  $U_{eq}$  of the carbon atom to which the hydrogen atom is attached), and their positions refined as “riding” atoms. After completing the initial structure solution of complexes **[5]**( $SbF_6$ ) and **[5]**( $SbF_6$ )<sub>2</sub>, it was found that ca. 10% and 37% of the total cell volume was filled with disordered solvent, accounting for 84 and 386 electrons per unit cell, respectively. These solvent molecules, likely to be  $Et_2O$  in partial occupation in case of **[5]**( $SbF_6$ ) and  $CH_2Cl_2$ /toluene for **[5]**( $SbF_6$ )<sub>2</sub>, could not be well-modelled in terms of atomic sites, and the SQUEEZE procedure [72] was, therefore, applied to the data to remove this contribution. CCDC 2170556-2170559 contains the supplementary crystallographic data for the structures unveiled in this paper. These data can be obtained, free of charge, from the Cambridge Crystallographic Data Centre via [www.ccdc.cam.ac.uk/data\\_request/cif](http://www.ccdc.cam.ac.uk/data_request/cif).

#### 4. Conclusions

Following a first study on the thiourea derivatives, we then conducted a complete exploration of the redox behavior of a series of transition-metal complexes supported by the NHC ligand  $IMes^{(NMe_2)_2}$  (**1**), whose carbenic heterocycle is substituted by two dimethylamino groups. The ability of ligand **1** to act as a redox-active ligand is shown through different spectroscopic, and even crystallographic, techniques on the oxidized forms of the complexes. In a similar behavior to the thiourea derivative, the two dimethylamino groups in **1** play a critical role in the stabilization of the mono-oxidized ligand  $[IMes^{(NMe_2)_2}]^{\bullet+}$  (**1**<sup>•+</sup>) in the complexes, by allowing an efficient delocalization of the spin density over the diaminoethene backbone. Conversely, the bis-oxidized state of the ligand is not generated

in these complexes. The oxidation process of the NHC ligand is shown to have a profound effect on its overall electronic donation, leading to a new redox-switchable NHC. An obvious limitation of this ligand is a relatively high oxidation potential, which would limit its implementation in organometallic catalysis. We are, therefore, considering further developments, aimed at improving both the accessibility and stability of the oxidized forms of the NHC ligands, by changing the nature and location of the redox-active moiety, the NHC platform, and/or the denticity of the NHC ligand. Investigations along those lines are currently being performed in our laboratories.

**Supplementary Materials:** The following supporting information can be downloaded at: <https://www.mdpi.com/article/10.3390/molecules27123776/s1>: SI containing IR, UV-Vis, and NMR spectra, crystallographic information and the atomic coordinates of the calculated structures [73–76].

**Author Contributions:** Conceptualization, M.R., V.M. and V.C.; investigation, M.R., S.B., L.R., A.S.-S., L.V., N.L., J.-M.M., D.A.V. and V.M.; formal analysis, M.R., S.B., L.R., A.S.-S., L.V., N.L., J.-M.M., D.A.V., V.M. and V.C.; methodology, M.R., J.-M.M., D.A.V., V.M. and V.C.; supervision, V.M. and V.C.; funding acquisition, V.M. and V.C.; writing—original draft, J.-M.M., D.A.V., V.M. and V.C.; writing—review & editing, M.R., S.B., L.R., A.S.-S., L.V., N.L., J.-M.M., D.A.V., V.M. and V.C. All authors have read and agreed to the published version of the manuscript.

**Funding:** Financial support from the CNRS, the CEA, and the IR RENARD federation (IR-RPE CNRS 3443) is gratefully acknowledged. M.R. thanks the “Région Midi-Pyrénées” for a PhD fellowship.

**Data Availability Statement:** Data is available in the Supplementary Material.

**Conflicts of Interest:** The authors declare no conflict of interest.

**Sample Availability:** Samples of the compounds might be available from the authors.

## References

1. Arduengo, A.J.; Harlow, R.L.; Kline, M. A stable crystalline carbene. *J. Am. Chem. Soc.* **1991**, *113*, 361–363. [[CrossRef](#)]
2. Herrmann, W.A.; Elison, M.; Fischer, J.; Köcher, C.; Artus, G.R.J. Metal Complexes of N-Heterocyclic Carbenes—A New Structural Principle for Catalysts in Homogeneous Catalysis. *Angew. Chem. Int. Ed. Engl.* **1995**, *34*, 2371–2374. [[CrossRef](#)]
3. Hopkinson, M.N.; Richter, C.; Schedler, M.; Glorius, F. An overview of N-heterocyclic carbenes. *Nature* **2014**, *510*, 485–496. [[CrossRef](#)] [[PubMed](#)]
4. Zhao, Q.; Meng, G.; Nolan, S.P.; Szostak, M. N-Heterocyclic Carbene Complexes in C–H Activation Reactions. *Chem. Rev.* **2020**, *120*, 1981–2048. [[CrossRef](#)] [[PubMed](#)]
5. Romain, C.; Bellemin-Laponnaz, S.; Dagorne, S. Recent progress on NHC-stabilized early transition metal (group 3–7) complexes: Synthesis and applications. *Coord. Chem. Rev.* **2020**, *422*, 213411. [[CrossRef](#)]
6. Foster, D.; Borhanuddin, S.M.; Dorta, R. Designing successful monodentate N-heterocyclic carbene ligands for asymmetric metal catalysis. *Dalton Trans.* **2021**, *50*, 17467–17477. [[CrossRef](#)] [[PubMed](#)]
7. Peris, E. Smart N-Heterocyclic Carbene Ligands in Catalysis. *Chem. Rev.* **2018**, *118*, 9988–10031. [[CrossRef](#)]
8. Visbal, R.; Gimeno, M.C. N-heterocyclic carbene metal complexes: Photoluminescence and applications. *Chem. Soc. Rev.* **2014**, *43*, 3551–3574. [[CrossRef](#)]
9. Mora, M.; Gimeno, M.C.; Visbal, R. Recent advances in gold–NHC complexes with biological properties. *Chem. Soc. Rev.* **2019**, *48*, 447–462. [[CrossRef](#)]
10. Smith, C.A.; Narouz, M.R.; Lummis, P.A.; Singh, I.; Nazemi, A.; Li, C.-H.; Crudden, C.M. N-Heterocyclic Carbenes in Materials Chemistry. *Chem. Rev.* **2019**, *119*, 4986–5056. [[CrossRef](#)]
11. Huynh, H.V. Electronic Properties of N-Heterocyclic Carbenes and Their Experimental Determination. *Chem. Rev.* **2018**, *118*, 9457–9492. [[CrossRef](#)] [[PubMed](#)]
12. Gomez-Suarez, A.; Nelson, D.J.; Nolan, S.P. Quantifying and understanding the steric properties of N-heterocyclic carbenes. *Chem. Commun.* **2017**, *53*, 2650–2660. [[CrossRef](#)] [[PubMed](#)]
13. Tumanskii, B.; Sheberla, D.; Molev, G.; Apeloig, Y. Dual Character of Arduengo Carbene–Radical Adducts: Addition versus Coordination Product. *Angew. Chem. Int. Ed.* **2007**, *46*, 7408–7411. [[CrossRef](#)] [[PubMed](#)]
14. Chirila, A.; Das, B.G.; Kuijpers, P.F.; Sinha, V.; de Bruin, B. Application of Stimuli-Responsive and “Non-innocent” Ligands in Base Metal Catalysis. In *Non-Noble Metal Catalysis*; Wiley: Weinheim, Germany, 2019; pp. 1–31. [[CrossRef](#)]
15. Broere, D.L.J.; Plessius, R.; van der Vlugt, J.I. New avenues for ligand-mediated processes—Expanding metal reactivity by the use of redox-active catechol, o-aminophenol and o-phenylenediamine ligands. *Chem. Soc. Rev.* **2015**, *44*, 6886–6915. [[CrossRef](#)]
16. Luca, O.R.; Crabtree, R.H. Redox-active ligands in catalysis. *Chem. Soc. Rev.* **2013**, *42*, 1440–1459. [[CrossRef](#)] [[PubMed](#)]

17. Lyaskovskyy, V.; de Bruin, B. Redox Non-Innocent Ligands: Versatile New Tools to Control Catalytic Reactions. *ACS Catal.* **2012**, *2*, 270–279. [[CrossRef](#)]
18. Dzik, W.I.; van der Vlugt, J.I.; Reek, J.N.H.; de Bruin, B. Ligands that Store and Release Electrons during Catalysis. *Angew. Chem. Int. Ed.* **2011**, *50*, 3356–3358. [[CrossRef](#)]
19. Klenk, S.; Rupf, S.; Suntrup, L.; van der Meer, M.; Sarkar, B. The Power of Ferrocene, Mesoionic Carbenes, and Gold: Redox-Switchable Catalysis. *Organometallics* **2017**, *36*, 2026–2035. [[CrossRef](#)]
20. Hettmanczyk, L.; Suntrup, L.; Klenk, S.; Hoyer, C.; Sarkar, B. Heteromultimetallic Complexes with Redox-Active Mesoionic Carbenes: Control of Donor Properties and Redox-Induced Catalysis. *Chem. Eur. J.* **2017**, *23*, 576–585. [[CrossRef](#)]
21. Labande, A.; Debono, N.; Sournia-Saquet, A.; Daran, J.-C.; Poli, R. Oxidation-promoted activation of a ferrocene C-H bond by a rhodium complex. *Dalton Trans.* **2013**, *42*, 6531–6537. [[CrossRef](#)]
22. Rosen, E.L.; Varnado, C.D.; Tennyson, A.G.; Khramov, D.M.; Kamplain, J.W.; Sung, D.H.; Cresswell, P.T.; Lynch, V.M.; Bielawski, C.W. Redox-Active N-Heterocyclic Carbenes: Design, Synthesis, and Evaluation of Their Electronic Properties. *Organometallics* **2009**, *28*, 6695–6706. [[CrossRef](#)]
23. Vanicek, S.; Podewitz, M.; Stubbe, J.; Schulze, D.; Kopacka, H.; Wurst, K.; Müller, T.; Lippmann, P.; Haslinger, S.; Schottenberger, H.; et al. Highly Electrophilic, Catalytically Active and Redox-Responsive Cobaltoceniumyl and Ferrocenyl Triazolylidene Coinage Metal Complexes. *Chem. Eur. J.* **2018**, *24*, 3742–3753. [[CrossRef](#)] [[PubMed](#)]
24. Tennyson, A.G.; Ono, R.J.; Hudnall, T.W.; Khramov, D.M.; Er, J.A.V.; Kamplain, J.W.; Lynch, V.M.; Sessler, J.L.; Bielawski, C.W. Quinobis(imidazolylidene): Synthesis and Study of an Electron-Configurable Bis(N-Heterocyclic Carbene) and Its Bimetallic Complexes. *Chem. Eur. J.* **2010**, *16*, 304–315. [[CrossRef](#)] [[PubMed](#)]
25. Ahumada, G.; Ryu, Y.; Bielawski, C.W. Potentiostatically Controlled Olefin Metathesis. *Organometallics* **2020**, *39*, 1744–1750. [[CrossRef](#)]
26. Lastovickova, D.N.; Teator, A.J.; Shao, H.; Liu, P.; Bielawski, C.W. A redox-switchable ring-closing metathesis catalyst. *Inorg. Chem. Front.* **2017**, *4*, 1525–1532. [[CrossRef](#)]
27. Harris, C.F.; Bayless, M.B.; van Leest, N.P.; Bruch, Q.J.; Livesay, B.N.; Bacsá, J.; Hardcastle, K.I.; Shores, M.P.; de Bruin, B.; Soper, J.D. Redox-Active Bis(phenolate) N-Heterocyclic Carbene [OCO] Pincer Ligands Support Cobalt Electron Transfer Series Spanning Four Oxidation States. *Inorg. Chem.* **2017**, *56*, 12421–12435. [[CrossRef](#)]
28. Harris, C.F.; Kuehner, C.S.; Bacsá, J.; Soper, J.D. Photoinduced Cobalt(III)–Trifluoromethyl Bond Activation Enables Arene C–H Trifluoromethylation. *Angew. Chem. Int. Ed.* **2018**, *57*, 1311–1315. [[CrossRef](#)]
29. Gravogl, L.; Heinemann, F.W.; Munz, D.; Meyer, K. An Iron Pincer Complex in Four Oxidation States. *Inorg. Chem.* **2020**, *59*, 5632–5645. [[CrossRef](#)]
30. Kunert, R.; Philouze, C.; Jarjays, O.; Thomas, F. Stable M(II)-Radicals and Nickel(III) Complexes of a Bis(phenol) N-Heterocyclic Carbene Chelated to Group 10 Metal Ions. *Inorg. Chem.* **2019**, *58*, 8030–8044. [[CrossRef](#)]
31. Romain, C.; Choua, S.; Collin, J.-P.; Heinrich, M.; Bailly, C.; Karmazin-Brelot, L.; Bellemin-Laponnaz, S.; Dagorne, S. Redox and Luminescent Properties of Robust and Air-Stable N-Heterocyclic Carbene Group 4 Metal Complexes. *Inorg. Chem.* **2014**, *53*, 7371–7376. [[CrossRef](#)]
32. Ruiz-Zambrana, C.; Gutiérrez-Blanco, A.; Gonell, S.; Poyatos, M.; Peris, E. Redox-Switchable Cycloisomerization of Alkynoic Acids with Naphthalenediimide-Derived N-Heterocyclic Carbene Complexes. *Angew. Chem. Int. Ed.* **2021**, *60*, 20003–20011. [[CrossRef](#)] [[PubMed](#)]
33. Ruiz-Zambrana, C.; Poyatos, M.; Peris, E. A Redox-Switchable Gold(I) Complex for the Hydroamination of Acetylenes: A Convenient Way for Studying Ligand-Derived Electronic Effects. *ACS Catal.* **2022**, *12*, 4465–4472. [[CrossRef](#)]
34. Crabtree, R.H. Multifunctional ligands in transition metal catalysis. *New J. Chem.* **2011**, *35*, 18–23. [[CrossRef](#)]
35. Ruamps, M.; Bastin, S.; Rechinat, L.; Sournia-Saquet, A.; Valyaev, D.A.; Mouesca, J.-M.; Lugan, N.; Maurel, V.; Cesar, V. Unveiling the redox-active character of imidazolin-2-thiones derived from amino-substituted N-heterocyclic carbenes. *Chem. Commun.* **2018**, *54*, 7653–7656. [[CrossRef](#)] [[PubMed](#)]
36. Zhang, Y.; César, V.; Storch, G.; Lugan, N.; Lavigne, G. Skeleton Decoration of NHCs by Amino Groups and its Sequential Booster Effect on the Palladium-Catalyzed Buchwald–Hartwig Amination. *Angew. Chem. Int. Ed.* **2014**, *53*, 6482–6486. [[CrossRef](#)]
37. Zhang, Y.; César, V.; Lavigne, G. Efficient and Versatile Buchwald–Hartwig Amination of (Hetero)aryl Chlorides Using the Pd–PEPPSI–IPr(NMe)<sub>2</sub> Precatalyst in the Presence of Carbonate Base. *Eur. J. Org. Chem.* **2015**, *2015*, 2042–2050. [[CrossRef](#)]
38. Zhang, Y.; Lavigne, G.; César, V. Buchwald–Hartwig Amination of (Hetero)Aryl Tosylates Using a Well-Defined N-Heterocyclic Carbene/Palladium(II) Precatalyst. *J. Org. Chem.* **2015**, *80*, 7666–7673. [[CrossRef](#)]
39. César, V.; Zhang, Y.; Kośnik, W.; Zieliński, A.; Rajkiewicz, A.A.; Ruamps, M.; Bastin, S.; Lugan, N.; Lavigne, G.; Grela, K. Ruthenium Catalysts Supported by Amino-Substituted N-Heterocyclic Carbene Ligands for Olefin Metathesis of Challenging Substrates. *Chem. Eur. J.* **2017**, *23*, 1950–1955. [[CrossRef](#)]
40. Zhang, Y.; Lavigne, G.; Lugan, N.; César, V. Buttressing Effect as a Key Design Principle towards Highly Efficient Palladium/N-Heterocyclic Carbene Buchwald–Hartwig Amination Catalysts. *Chem. Eur. J.* **2017**, *23*, 13792–13801. [[CrossRef](#)]
41. Broggi, J.; Terme, T.; Vanelle, P. Organic Electron Donors as Powerful Single-Electron Reducing Agents in Organic Synthesis. *Angew. Chem. Int. Ed.* **2014**, *53*, 384–413. [[CrossRef](#)]
42. Doni, E.; Murphy, J.A. Evolution of neutral organic super-electron-donors and their applications. *Chem. Commun.* **2014**, *50*, 6073–6087. [[CrossRef](#)] [[PubMed](#)]

43. Danopoulos, A.A.; Simler, T.; Braunstein, P. N-Heterocyclic Carbene Complexes of Copper, Nickel, and Cobalt. *Chem. Rev.* **2019**, *119*, 3730–3961. [[CrossRef](#)] [[PubMed](#)]
44. Connelly, N.G.; Geiger, W.E. Chemical Redox Agents for Organometallic Chemistry. *Chem. Rev.* **1996**, *96*, 877–910. [[CrossRef](#)]
45. Kelly, R.A., III; Clavier, H.; Giudice, S.; Scott, N.M.; Stevens, E.D.; Bordner, J.; Samardjiev, I.; Hoff, C.D.; Cavallo, L.; Nolan, S.P. Determination of N-Heterocyclic Carbene (NHC) Steric and Electronic Parameters using the [(NHC)Ir(CO)<sub>2</sub>Cl] System. *Organometallics* **2007**, *27*, 202–210. [[CrossRef](#)]
46. Wolf, S.; Plenio, H. Synthesis of (NHC)Rh(cod)Cl and (NHC)RhCl(CO)<sub>2</sub> complexes—Translation of the Rh- into the Ir-scale for the electronic properties of NHC ligands. *J. Organomet. Chem.* **2009**, *694*, 1487–1492. [[CrossRef](#)]
47. Sanderson, M.D.; Kamplain, J.W.; Bielawski, C.W. Quinone-Annulated N-Heterocyclic Carbene–Transition-Metal Complexes: Observation of  $\pi$ -Backbonding Using FT-IR Spectroscopy and Cyclic Voltammetry. *J. Am. Chem. Soc.* **2006**, *128*, 16514–16515. [[CrossRef](#)]
48. Benhamou, L.; Vujkovic, N.; César, V.; Gornitzka, H.; Lugan, N.I.; Lavigne, G. Facile Derivatization of a “Chemo-active” NHC Incorporating an Enolate Backbone and Relevant Tuning of Its Electronic Properties. *Organometallics* **2010**, *29*, 2616–2630. [[CrossRef](#)]
49. Ruamps, M.; Lugan, N.; César, V. A Cationic N-Heterocyclic Carbene Containing an Ammonium Moiety. *Organometallics* **2017**, *36*, 1049–1055. [[CrossRef](#)]
50. Braun, M.; Frank, W.; Ganter, C. Reactivity of an Oxalamide-Based N-Heterocyclic Carbene. *Organometallics* **2012**, *31*, 1927–1934. [[CrossRef](#)]
51. Buhl, H.; Ganter, C. Tuning the electronic properties of an N-heterocyclic carbene by charge and mesomeric effects. *Chem. Commun.* **2013**, *49*, 5417–5419. [[CrossRef](#)]
52. Khramov, D.M.; Lynch, V.M.; Bielawski, C.W. N-Heterocyclic Carbene–Transition Metal Complexes: Spectroscopic and Crystallographic Analyses of  $\pi$ -Back-bonding Interactions. *Organometallics* **2007**, *26*, 6042–6049. [[CrossRef](#)]
53. Ryu, Y.; Ahumada, G.; Bielawski, C.W. Redox- and light-switchable N-heterocyclic carbenes: A “soup-to-nuts” course on contemporary structure–activity relationships. *Chem. Commun.* **2019**, *55*, 4451–4466. [[CrossRef](#)] [[PubMed](#)]
54. Buchgraber, P.; Toupet, L.; Guerschais, V. Syntheses, Properties, and X-ray Crystal Structures of Piano-Stool Iron Complexes Bearing an N-Heterocyclic Carbene Ligand. *Organometallics* **2003**, *22*, 5144–5147. [[CrossRef](#)]
55. Zheng, J.; Elangovan, S.; Valyaev, D.A.; Brousses, R.; César, V.; Sortais, J.-B.; Darcel, C.; Lugan, N.; Lavigne, G. Hydrosilylation of Aldehydes and Ketones Catalyzed by Half-Sandwich Manganese(I) N-Heterocyclic Carbene Complexes. *Adv. Synth. Catal.* **2014**, *356*, 1093–1097. [[CrossRef](#)]
56. Allen, F.H.; Kennard, O.; Watson, D.G.; Brammer, L.; Orpen, A.G.; Taylor, R. Tables of bond lengths determined by X-ray and neutron diffraction. Part 1. Bond lengths in organic compounds. *J. Chem. Soc. Perkin Trans. 2* **1987**, S1–S19. [[CrossRef](#)]
57. Brousses, R.; Maurel, V.; Mouesca, J.-M.; César, V.; Lugan, N.; Valyaev, D.A. Half-sandwich manganese complexes Cp(CO)<sub>2</sub>Mn(NHC) as redox-active organometallic fragments. *Dalton Trans.* **2021**, *50*, 14264–14272. [[CrossRef](#)]
58. Grineva, A.A.; Valyaev, D.A.; César, V.; Filippov, O.A.; Khrustalev, V.N.; Nefedov, S.E.; Lugan, N. Oxidative Coupling of Anionic Abnormal N-Heterocyclic Carbenes: Efficient Access to Janus-Type 4,4′-Bis(2H-imidazol-2-ylidene)s. *Angew. Chem. Int. Ed.* **2018**, *57*, 7986–7991. [[CrossRef](#)]
59. Wu, K.; Conger, M.A.; Waterman, R.; Liptak, M.; Geiger, W.E. Electrochemical and structural characterization of a radical cation formed by one-electron oxidation of a cymantrene complex containing an N-heterocyclic carbene ligand. *Polyhedron* **2019**, *157*, 442–448. [[CrossRef](#)]
60. Buhaibeh, R.; Duhayon, C.; Valyaev, D.A.; Sortais, J.-B.; Canac, Y. Cationic PCP and PCN NHC Core Pincer-Type Mn(I) Complexes: From Synthesis to Catalysis. *Organometallics* **2021**, *40*, 231–241. [[CrossRef](#)]
61. Ding, M.; Cutsail, G.E., III; Aravena, D.; Amoja, M.; Rouzières, M.; Dechambenoit, P.; Losovyj, Y.; Pink, M.; Ruiz, E.; Clérac, R.; et al. A low spin manganese(IV) nitride single molecule magnet. *Chem. Sci.* **2016**, *7*, 6132–6140. [[CrossRef](#)]
62. Telser, J. EPR Interactions—Zero-Field Splittings. *eMagRes* **2017**, *6*, 207–234. [[CrossRef](#)]
63. Bertrand, P. Spectrum Intensity, Saturation, Spin-Lattice Relaxation. In *Electron Paramagnetic Resonance Spectroscopy: Fundamentals*; Bertrand, P., Ed.; Springer International Publishing: Cham, Switzerland, 2020; pp. 155–196. [[CrossRef](#)]
64. Yasuda, S.; Yorimitsu, H.; Oshima, K. Synthesis of Aryliron Complexes by Palladium-Catalyzed Transmetalation between [CpFe(CO)<sub>2</sub>I] and Aryl Grignard Reagents and Their Chemistry Directed toward Organic Synthesis. *Organometallics* **2008**, *27*, 4025–4027. [[CrossRef](#)]
65. Guillon, C.; Vierling, P. Unexpected formation of novel benzofuran-yl-substituted ferrocenes by action of p-benzoquinone on 1,1′-bis-acylferrocene. *J. Organomet. Chem.* **1994**, *464*, C42–C44. [[CrossRef](#)]
66. Valyaev, D.A.; Uvarova, M.A.; Grineva, A.A.; César, V.; Nefedov, S.N.; Lugan, N. Post-coordination backbone functionalization of an imidazol-2-ylidene and its application to synthesize heteropolymetallic complexes incorporating the ambidentate IMesCO<sub>2</sub>-ligand. *Dalton Trans.* **2016**, *45*, 11953–11957. [[CrossRef](#)]
67. Fulmer, G.R.; Miller, A.J.M.; Sherden, N.H.; Gottlieb, H.E.; Nudelman, A.; Stoltz, B.M.; Bercaw, J.E.; Goldberg, K.I. NMR Chemical Shifts of Trace Impurities: Common Laboratory Solvents, Organics, and Gases in Deuterated Solvents Relevant to the Organometallic Chemist. *Organometallics* **2010**, *29*, 2176–2179. [[CrossRef](#)]
68. Stoll, S.; Schweiger, A. EasySpin, a comprehensive software package for spectral simulation and analysis in EPR. *J. Magn. Reson.* **2006**, *178*, 42–55. [[CrossRef](#)]



69. Farrugia, L. WinGX and ORTEP for Windows: An update. *J. Appl. Crystallogr.* **2012**, *45*, 849–854. [[CrossRef](#)]
70. Altomare, A.; Cascarano, G.; Giacovazzo, C.; Guagliardi, A.; Burla, M.C.; Polidori, G.; Camalli, M. SIR92—A program for automatic solution of crystal structures by direct methods. *J. Appl. Crystallogr.* **1994**, *27*, 435. [[CrossRef](#)]
71. Sheldrick, G. SHELXT—Integrated space-group and crystal-structure determination. *Acta Crystallogr. Sect. A* **2015**, *71*, 3–8. [[CrossRef](#)]
72. van der Sluis, P.; Spek, A.L. BYPASS: An effective method for the refinement of crystal structures containing disordered solvent regions. *Acta Crystallogr. Sect. A* **1990**, *46*, 194–201. [[CrossRef](#)]
73. te Velde, G.; Baerends, E.J. Numerical integration for polyatomic systems. *J. Comput. Phys.* **1992**, *99*, 84–98. [[CrossRef](#)]
74. Vosko, S.H.; Wilk, L.; Nusair, M. Accurate spin-dependent electron liquid correlation energies for local spin density calculations: A critical analysis. *Can. J. Phys.* **1980**, *58*, 1200–1211. [[CrossRef](#)]
75. Becke, A.D. Density-functional exchange-energy approximation with correct asymptotic behavior. *Phys. Rev. A* **1988**, *38*, 3098–3100. [[CrossRef](#)] [[PubMed](#)]
76. Perdew, J.P. Density-functional approximation for the correlation energy of the inhomogeneous electron gas. *Phys. Rev. B* **1986**, *33*, 8822–8824. [[CrossRef](#)]